Università degli Studi di Padova

DIPARTIMENTO DI FISICA E ASTRONOMIA "GALILEO GALILEI"
Corso di Laurea in Astronomia

The Initial Mass-Final Mass Relation of low- and intermediate-mass stars: constraints to the Asymptotic Giant Branch phase

Candidate:
Stefano Giarratana

Thesis Advisor:
Prof. Paola Marigo

Thesis submitted in 2017

Contents

Chapter 1

Abstract

Stars with initial mass M_i in the range $0.9M_\odot \leq M_i \leq 6 - 9M_\odot$ end their lives as White Dwarfs (WDs) after the ejection of the upper layers through stellar winds. The masses of the white dwarf and the Zero Age Main Sequence (ZAMS) progenitor can be linked in the so-called Initial-Final Mass Relation (IFMR), a fundamental tool in both stellar evolution analysis and galaxy models. In fact, this semi-empirical law directly provides an estimate of the mass loss during the stellar lifetime and its dependence on stellar mass (figure 1.1 on the following page). Furthermore, the high-mass end of the IFMR suggests an upper value for the initial mass of stars developing a degenerate Carbon-Oxygen core: thus, it becomes a valid test to both the Type Ia SuperNovae (SNe) rates, through the determination of the additional amount of material a WD in a binary system has to accrete to reach the Chandrasekhar limit for the carbon deflagration (Marigo (2013)), and the Type II SNe rates, forcing the value of the critical mass which separates this catastrophic explosion from the WD production (Kalirai, Hansen, et al. (2008)).

The IFMR gives also an overall feedback to galaxy models: it can put constraints on the chemical evolution through the amount of metal-enriched gas brought back to the interstellar medium due to stellar winds (hence it can also enhance the understanding of star formation efficiency); it represents a primary input in the mass-to-light ratio of stellar population; it can be useful to estimate the distance and the age of globular clusters interpreting the luminosity function and modeling the cooling sequences of WDs (hence also a technique for measuring the age of the Galactic halo). Finally, the measurement of the fuel burnt during the thermal pulsing-asymptotic giant branch phase can be used to find the energy output of the star during this phase and thus the luminosity contribution of the asymptotic giant branch star populations to the integrated galaxy light.

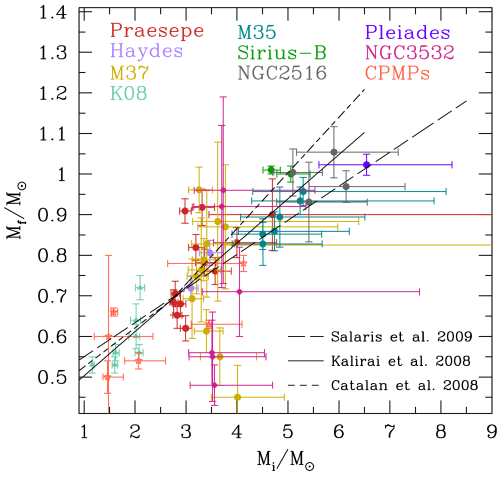

Figure 1.1: Predicted and semi-empirical IFMRs from Marigo (2013).

The first attempt for a IFMR was done by Weidemann in 1977, who discovered that the mass loss had been greatly understimated comparing the theoretical models for the mass loss at that time available with the observed masses of WDs in the Hyades and Pleiades. Subsequent works demonstrated that a nearly linear correlation between Main Sequence (MS) progenitor mass and WD mass occurs, so that higher-mass stars produce increasingly more massive WDs. However, in the last $\sim$ 20 years the amount of data has increased proving that the relation can't be linear in the full mass range (Cummings, Kalirai, Tremblay, and Ramirez-Ruiz (2015)) showing a shallower slope at higher masses.

Although the empirical resources are increased, the scatter has become significantly larger due to both an intrinsic effect, so that the stochastic nature of the mass loss, and the uncertainties caused by theoretical models, such as the stellar isochrones and the WD cooling sequences, which propagate the systematic errors to the cluster's age, metallicity (Z), amount of convective overshooting, thickness of the WD H/He layers, chemical composition of the degenerate core (Marigo (2013)). Thus, data from different groups of research processed adopting different evolutionary models are affected by relative systematic errors. However, a single valid model can't be reached since our understanding of some crucial processes, like the convection, is still incomplete.

In this thesis we analyse the dependencies which play a significant role in the IFMR in order to improve future models: the 2^{nd} dredge up, the 3^{rd} dredge up, the mass loss and the metallicity. This can be done comparing

the theoretical models with a uniform and wide set of semi-empirical data which covers the almost entire initial mass and metallicity ranges. In the chapter 2 we discuss the stellar evolution after the He-burning phase for stars with $0.9M_{\odot} \leq M_i \leq 6 - 9M_{\odot}$; in the chapter 3 we present the semi-empirical data and IFMR; the description of the theoretical models involved in the work and their agreement with the semi-empirical quantities are exposed in the chapter 4; finally, the summary and the conclusions are resumed in the chapter 5.

Chapter 2

Stellar Evolution

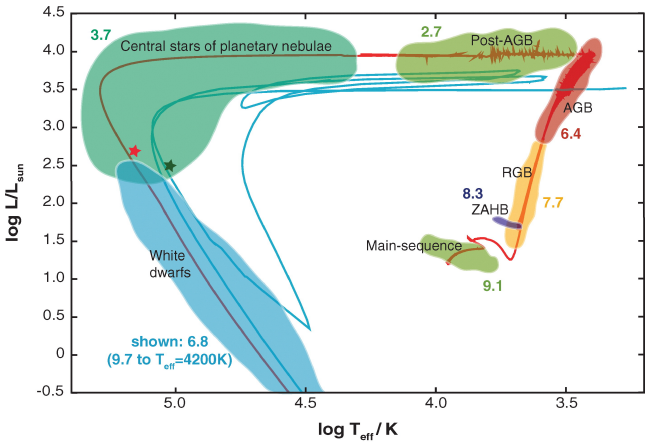

Herwig, F. 2005
Annu. Rev. Astron. Astrophys. 43: 435–79

Figure 2.1: Hertzsprung-Russell diagram of a $2M_{\odot}$ and solar metallicity star. Figure from Herwig (2005).

In this chapter we briefly discuss the stellar evolution after the Helium burning for stars with $0.9M_{\odot} \leq M_i \leq 6 - 9M_{\odot}$. We split this mass range into $M_i \leq 2M_{\odot}$ and $M_i \geq 2M_{\odot}$ for convenience: the first group includes the low-mass stars, that ignite helium (He) in degenerate conditions (the He-flash) during the RGB phase, while the second group contains the intermediate-mass stars, which avoid He core degeneracy. We refer to Herwig (2005) for the complete review of this phase. In figure 2.1 from Herwig (2005) the main phases are exposed in a Hertzsprung-Russell diagram of a $2M_{\odot}$ and solar metallicity star, from the main sequence to the WD phase. In the post-AGB section, wiggles in the track are caused by numerical convergence difficulties. The blue track shows a born-again evolution of the same mass.

The red and green stars mark the position of the central stars of planetary nebulae. The number for each evolutionary phase indicates the logarithm of the duration. Larger or smaller mass cases would have respectively smaller or larger evolutionary timescales.

2.1 The AGB Phase

The Asymptotic Giant Branch (AGB) phase starts whith the exhaustion of the He in the centre. The internal structure of the star now consists of an inert electron-degenerate Carbon-Oxygen (CO) core, surrounded by (from the center outwards) a He-burning shell, an inert thin He-rich shell, a H-burning shell and a convective envelope.

2.1.1 The Early AGB phase and the second Dredge-Up

Initially the He-burning shell is providing all the luminosity. Indeed, as the core is contracting and releasing gravitational energy, the He burning reaction rate increases, driving the expansion and the consequent cooling of the envelope. The effective temperature decreases while the luminosity increases (due to the larger radius): the star moves upwards and to the right in the Hertzsprung-Russell Diagram, approaching the Hayashi line. The H-burning shell is temporarily extinguished for stars with $M_i \geq 3 - 4M_\odot$ (Dominguez et al. (1999)) and the base of the convective envelope moves inwards causing a mixing of material which has previously undergone H-burning to the surface: the so-called 2^{nd} dredge-up. Thus, products such as ^{4}He and ^{14}N appear at the surface. This process does not take place in lower mass stars because the expansion induced by the He-shell is not sufficient to cool the H-shell enough (Dominguez et al. (1999)). At the end of the 2^{nd} dredge-up, the H-burning shell is restored. Now the star has two energy sources.

2.1.2 The TP-AGB phase

The energy generation rate per unit time per unit mass for a given nuclear reaction involving the i and j particles is $\epsilon_{ij} \propto T^\nu$, where T is the temperature and ν a constant. For the triple-α reaction the ν found is ~ 40, while for the H-burning it depends on the chain which dominates the He production: for the proton-proton (PP) chain $\nu \simeq 4$, for the CNO-cycle $\nu \simeq 18$. At the end of the early AGB phase, the energy sources are close together. Thus, due

to the large gap which occurs between the different T dependencies for the H-burning and the He-burning reactions, the structure becomes thermally unstable, leading to a process termed *thermal pulse cycle* (TP). Initially the H shell provides all the luminosity, until the instability takes place and the energy generation rate of the He shell has a dramatic increase, pushing outwards (by even a factor of 2 in radius) the H shell which disappears. The He-burning shell drives a convective pocket in the He-rich inert intershell, bringing the triple-α products upwards to the intershell region. This He-flash phase lasts for $\sim$ 100 years, then the He shell dies down and the intershell convective pocket disappears.

The 3rd Dredge-Up

As the opacity increases due to the lower T, the convective envelope penetrates into deeper regions. For stars with $M_i \geq 2M_{\odot}$, the convective upper layers and the region which previously was the convective intershell overlap, hence the convection can reach material produced by the He-flash nucleosynthesis. The process, called 3^{rd} *dredge-up* (or TDU), succeeds in mixing material enriched with ^{12}C, ^{4}He, ^{22}Ne, ^{19}F, ^{25}Mg and other s-process elements to the surface, leading to important nucleosynthesis (Iben and Truran (1978), Cristallo, Straniero, Gallino, et al. (2009)).

The 3^{rd} dredge-up is a fundamental process as it limits the growth of the CO core subtracting material that would otherwise be used to accrete the core. Thus its efficiency affects significantly the Initial-Final Mass Relation and it will be discussed in the section 4.2.1 on page 31.

The TDU lasts $\sim$ 100 years, then the star contracts and the H-shell is restored and provides all the luminosity for $\sim$ 10000 years. This phase is called *interpulse*. During the entire cycle the surface luminosity remains almost unchanged. Traditionally, the efficiency of the 3^{rd} dredge-up is calculated through the parameter:

$$\lambda = \frac{\Delta M_{dredge-up}}{\Delta M_c} \tag{2.1}$$

where $\Delta M_{dredge-up}$ is the dredged-up mass and ΔM_c is the core mass increment during the previous quiescent interpulse phase. A $\lambda = 0$ corresponds to an absence of dredge-up, and a $\lambda = 1$ means that all the material that the core accretes during the interpulse period is ejected after the dredge-up.

The Hot Bottom Burning

The AGB phase is responsible for many of the nuclei found in the universe. We can't discuss here all the unique nucleosynthesis which takes place during this phase, however, we must mention the *Hot Bottom Burning* (HBB). This process affects stars with a core mass $M_c > 0.8 M_\odot$ surrounded by an envelope with a mass $M_{env} > 2 M_\odot$ (Marigo (2013)), where the inner edge of the convective envelope penetrates the upper edge of the H-burning shell. We must stress that the minimum mass for the onset of the HBB is a function of the metallicity: at lower Z a lower stellar mass is needed for the HBB (Ventura and D'Antona (2005)). The temperature T is high enough for the H-burning nuclear reactions, so the nucleosynthesis starts also at the bottom of the envelope (Forestini and Charbonnel (1997)):

- As the ^{7}Be is produced by the PP chain, it is transported upwards to cooler regions before completing the nuclear reactions chain (PPII or PPIII) which would otherwise destroy it. There, through the electron capture, it turns into ^{7}Li. This process, termed Cameron-Fowler Beryllium Transport Mechanism, leads to a temporary super-rich Li phase.

- through the CNO cycle, the HBB converts the ^{12}C into ^{13}C and ^{14}N, increasing the ^{14}N abundance in the surface and thus preventing the formation of Carbon stars.

- The Ne−Na and the Mg−Al cycles can operate due to the suitable conditions, producing ^{23}Na through $^{22}\mathrm{Ne}\,(\mathrm{p},\gamma)\,^{23}\mathrm{Na}$ and ^{26}Al through $^{25}\mathrm{Mg}\,(\mathrm{p},\gamma)\,^{26}\mathrm{Al}$.

Furthermore, the HBB makes the observed luminosity brighter than expected by the classical $M_c - L$ relation (Bloecker and Schoenberner (1991)). Even if the HBB is fundamental for the unique nucleosynthesis provided, in this work we focus on the stellar mass during its lifetime, rather than on the chemical evolution, thus we will discuss the IFMR dependencies on the 2^{nd} dredge-up, 3^{rd} dredge-up, mass loss and metallicity.

2.2 The White Dwarf phase

The products of the AGB nucleosynthesis are released to the interstellar medium through stellar winds. The mechanism driving the ejection of large portion of mass is not completely understood, although some clues suggest that an essential role is performed by the dust particles while the star is

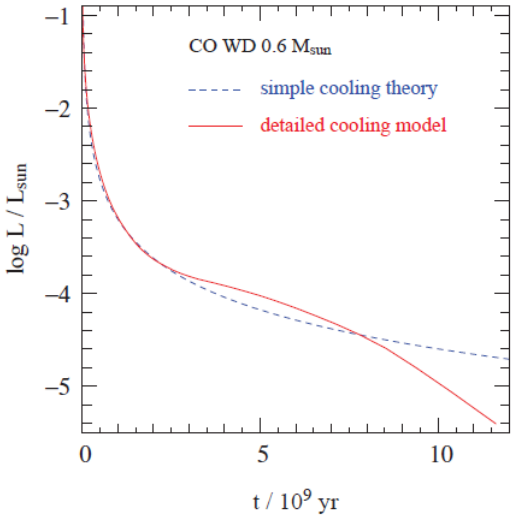

Figure 2.2: Predicted cooling curves for a CO white dwarf of $0.6M_{\odot}$.

ascending the AGB. In fact, during the TP-AGB phase, the pulsations induce shock waves in the stellar atmosphere, bringing gas to larger radii. Thus the density increases in the outer layers, where the temperature is significantly lower. These conditions make the dust particles condensation possible. The radiation coming out from the star is strong enough to easily accelerate these particles, causing a net outgoing mass flux. Hence, once the star enters the super-wind phase, the envelope is rapidly removed. When the mass of the H-rich envelope becomes sufficiently small (about $10^{-2} - 10^{-3}M_{\odot}$), the outer layers shrink and the star leaves the AGB; thus, the mass loss directly influences the TP-AGB phase itself: the more efficient is the process, the shorter will be the phase. Since the H-burning shell is still active and the star follows the $M_c - L$ relation, the luminosity remains almost unchanged while the effective temperature increases: the star draws an horizontal track on the Hertzsprung-Russell Diagram. However, the stellar structure is stable during this phase: the temperature increases because the removal of the outer gas leaves the deeper and hotter layers exposed. When the $T \geq 30000K$, a strong UV flux destoys the dust grains in the circumstellar envelope, dissociating the molecules and ionizing the gas. This phase is called *planetary nebula*. Finally, when $T \simeq 10^5 K$, the H-burning shell is extinguished. The remnant is called *white dwarf*, a star within which the electron degeneracy allows a stable structure even when it cools down.

Nuclear fusion no longer provides energy and the WD shines by radiating thermal energy, cooling at almost constant radius due to the electron degene-

racy and decreasing luminosity L. Observed WDs are found in a range around $\sim 0.6M_\odot$, which corresponds to a $\leq 2M_\odot$ progenitor mass. Thus, the great majority of the WDs are composed of C and O; those with $M < 0.45M_\odot$ are He WDs produced from low-mass stars which remove their envelopes already on the RGB phase; those with $M > 1.2M_\odot$ are ONe WDs, formed from stars with sufficient mass to develop a degenerate ONe cores after C-burning. We refer to Mestel (1952) for the thermal properties and the evolution of WDs.

In the interior of a WD the temperature gradient is small due to the very low L and the high thermal conductivity caused by the degenerate electrons, hence we can consider the temperature almost constant. However, the outer layers are non-degenerate and thus the energy must be transported through radiation according to the high opacity. Since the outer layers act to insulate the degenerate interior from outer space, a significant temperature gradient must exist. Assuming a transition point where the electron-degeneracy pressure of the interior equals the ideal gas pressure of the electrons in the outer layers, a Kramers opacity law $k = k_0 \rho T^{-7/2}$ (where ρ is the density, T the temperature and k_0 a constant), pressure P and temperature T approaching to zero at the surface, free bound absorption and *the mean molecular weigth per free electron* $\mu_e = 2$ in the envelope, the relation between the interior temperature T_c on the one hand, the luminosity and the mass on the other hand is:

$$T_c \approx 7.7 \times 10^7 K \left(\frac{L/L_\odot}{M/M_\odot} \right)^{2/7}. \tag{2.2}$$

The typical masses and luminosities are $M \simeq 0.6M_\odot$ and $L < 10^{-2}L_\odot$, thus the WDs have temperature approximately $T_c < 2 \times 10^7 K$. A simple model for the WDs cooling time t_{cool} was derived in Mestel (1952) using this quantities. Firstly, the only energy source available for the luminosity radiated away comes from the thermal energy stored in the non-degenerate ions, since there are no nuclear sources, no contraction and the internal energy of the electrons which fill their lowest energy state up to the Fermi level cannot change. Subsequently, assuming that non-degenerate ions behave as an ideal gas with specific heat per unit mass $c_v = \frac{3}{2}\mathcal{R}/\mu_{ion}$ with $\mathcal{R} = 8.31447 \times 10^7 ergg^{-1}K^{-1}$ the universal gas constant and μ_{ion} *mean atomic mass per ion*, the relation for a generic cooling time t_{cool} becomes:

$$t_{cool} \approx \frac{1.05 \times 10^8 yr}{\mu_{ion}} \left(\frac{L/L_\odot}{M/M_\odot} \right)^{-5/7}. \tag{2.3}$$

This approximate cooling law shows that more massive WDs evolve more slowly, because more thermal energy is stored in their interior ions, while

t_{cool} is smaller for more luminous WDs. Moreover, increasing the μ_{ion} at constant total mass decreases the cooling time since fewer ions per unit mass are available. For a CO white dwarf composed with the same amount of C and O a $\mu_{ion} \approx 14$ is found. However, this simple cooling law seems to be unsuitable as it predicts cooling times larger than the age of the Universe when $L < 10^{-5} L_{\odot}$. More recent models take into account the effects of the non-degenerate envelope contraction, the Coulomb interactions and the *crystallization*: as the WD cools, the ions settle into a lattice structure due to the increased interactions, releasing heat. Thus $c_v > \frac{3}{2}\mathcal{R}/\mu_{ion}$ and t_{cool} results larger. Subsequently, once the crystallization is almost complete, c_v decreases and cooling speeds up. The two models are shown in figure 2.2 on page 13 for a CO white dwarf of $0.6 M_{\odot}$.

Chapter 3

Semi-Empirical Initial Final Mass Relation

The techniques to measure the masses of WDs are described in Kalirai, Hansen, et al. (2008):

- dynamical mass can be calculated from the orbit in a binary system;
- gravitational redshift, if the radial velocity is known, through the H_α Balmer Line;
- pulsation mode analysis for very hot WDs;
- fits to the mass-radius relation for WD with trigonometric paralaxes;
- fitting the Balmer lines of the spectrum to model atmospheres (Bergeron, Saffer, and Liebert (1992)).

Concerning the latter method, we recommend Salaris et al. (2009) for the full description: through the spectrum analysis the WD surface gravity g and the effective temperature T_{eff} can be derived; subsequently an interpolation within a grid of theoretical WD models provides the final mass M_f and the cooling age t_{cool} of the WD. The cluster age $t_{cluster}$ is inferred fitting the turn-off luminosity in the Color-Magnitude Diagram (CMD) with independent theoretical isochrones. Subtracting the t_{cool} to the $t_{cluster}$ gives the lifetime t_{MS} of the progenitor star from the Main Sequence to the top of the Asymptotic Giant Branch. Finally, the progenitor mass M_i is obtained using the mass-lifetime relationships from theoretical stellar evolution models. As said in chapter 1 on page 5, theoretical models bring unavoidable systematic errors in the estimate of $t_{cluster}$, metallicity (Z), amount of convective overshooting,

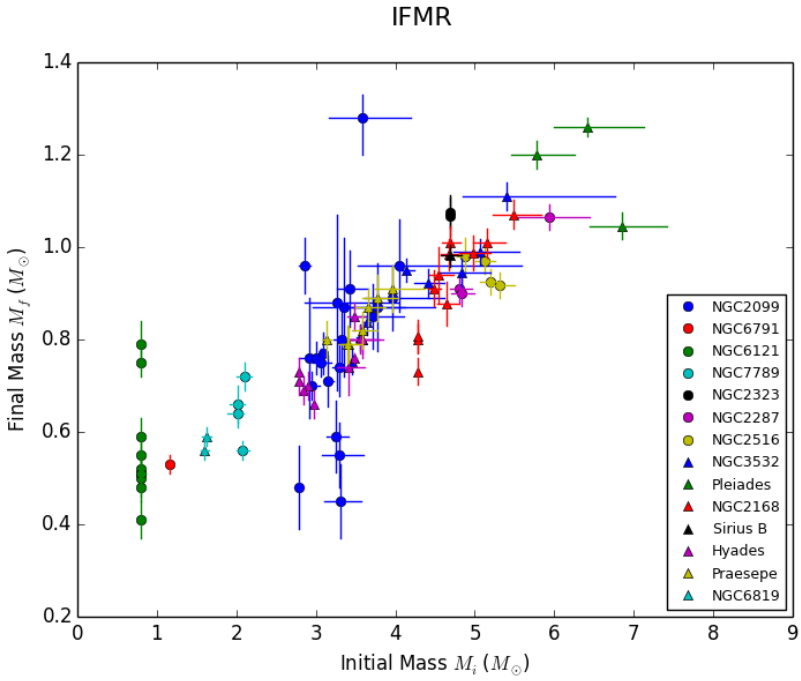

Figure 3.1: Semi-empirical IFMR from table 3.1 on page 21.

thickness of the WD H/He layers, chemical composition of the degenerate core (Marigo (2013)).

In this thesis we use the observations and results provided by the prof. Jason S. Kalirai (Space Telescope Science Institute, Baltimore, USA) and prof. Jeffrey D. Cummings (Center for Astrophysical Sciences, John Hopkins University, Baltimore, USA) with a wide set of papers from the year 2001 up to nowadays (figure 3.1), in order to get the ranges for the age, the metallicity, the initial and final masses as wider and more uniform as possible. Before the description of the clusters analysed in this thesis, we want to stress that this method leads as usual to unavoidable limits: first of all, during the years the human knowledge has been improving, so the last results must be naturally considered as more accurate; secondly, consistency is not yet fully achieved since the isochrones used to determine $t_{cluster}$ should be computed according to the evolutionary tracks adopted to infer M_i and all the cluster ages should be determined with the same method (Salaris et al. (2009)); finally, the solar metallicity is changed from $Z_\odot = 0.02$, assumed at the time of the first observations, to $Z_\odot = 0.0152$. As a general rule, we give the priority to the more recent results, to the $t_{cluster}$ derived with the PARSEC code (see Bressan et al. (2012)) and we assume the solar metallicity as $Z_\odot = 0.0152$. Here below the clusters analysed and their characteristics are presented: age,

metallicity, isochrones used for the $t_{cluster}$ and models for t_{cool} for the WDs which belong to that cluster. For more information we recommend to consult the references.

- **NGC2099**: analysed in Kalirai, Richer, Reitzel, et al. (2005),Cummings, Kalirai, Tremblay, and Ramirez-Ruiz (2015) and Cummings, Kalirai, Tremblay, Ramirez-Ruiz, and Bergeron (2016). It has an age of (520 ± 50) Myr and $[Fe/H] = 0.09$ (Kalirai, Ventura, et al. (2001)). The $t_{cluster}$ was calculated with the PARSEC code (Bressan et al. (2012)), the t_{cool} and the M_f with Fontaine, Brassard, and Bergeron (2001) for lower mass WD ($< 1.10 M_{\odot}$) and with Althaus et al. (2007) for massive WDs.

- **NGC6791**: analysed in Kalirai, Bergeron, et al. (2007) and Kalirai, Hansen, et al. (2008). The age is 8.5 Gyr and $[Fe/H] = 0.37$ (and corrected in Kalirai, Saul Davis, et al. (2009) in $[Fe/H] = 0.40$). $t_{cluster}$ was calculated with VandenBerg, Bergbusch, and Dowler (2006), t_{cool} and M_f with Fontaine, Brassard, and Bergeron (2001). The initial masses were calculated with Hurley, Pols, and Tout (2000).

- **NGC6121**: or M4, analysed in Kalirai, Saul Davis, et al. (2009). Age of ~ 12 Gyr (fixed for Milky Way globular cluster) and $[Fe/H] = -1.10$ (very low metallicity, useful to set a wide range for Z in this work). t_{cool} and M_f were calculated with Fontaine, Brassard, and Bergeron (2001); the initial masses were fixed at $M_i = (0.80 \pm 0.05) M_{\odot}$.

- **NGC6819**: analysed in Kalirai, Hansen, et al. (2008) and Kalirai, Marigo, and Tremblay (2014). The age of the cluster $t_{cluster}$ is 2.5 Gyr and the metallicity $[Fe/H] = 0.049$ (Kalirai, Richer, Fahlman, et al. (2001) and Kalirai, Hansen, et al. (2008)). The initial masses followed from models by Bressan et al. (2012), the remnant masses and t_{cool} from Bergeron, Saffer, and Liebert (1992) corrected with Tremblay and Bergeron (2009).

- **NGC7789**: analysed in Kalirai, Hansen, et al. (2008) and Kalirai, Marigo, and Tremblay (2014). The age of the cluster $t_{cluster}$ is 1.4 Gyr and the metallicity $[Fe/H] = -0.035$ (Kalirai, Richer, Fahlman, et al. (2001) and Kalirai, Hansen, et al. (2008)). The initial masses followed from models by Bressan et al. (2012), the remnant masses and t_{cool} from Bergeron, Saffer, and Liebert (1992) corrected with Tremblay and Bergeron (2009).

- **NGC2323**: analysed in Cummings, Kalirai, Tremblay, and Ramirez-Ruiz (2016). The age of (115 ± 20) Myr was found with the PARSEC code (Bressan et al. (2012)). It has solar metallicity $[Fe/H] = 0.00$ (described in Kalirai, Fahlman, et al. (2003)). t_{cool} and M_f were found with Fontaine, Brassard, and Bergeron (2001) for lower mass WD ($< 1.10 M_{\odot}$), with Althaus et al. (2007) for massive WDs. M_i determined with Bressan et al. (2012).

- **NGC2287**: analysed in Cummings, Kalirai, Tremblay, and Ramirez-Ruiz (2016). The age of (205 ± 30) My was found with the PARSEC code (Bressan et al. (2012)). It has solar metallicity $[Fe/H] = 0.00$. M_i determined with Bressan et al. (2012). t_{cool} and M_f were found with Fontaine, Brassard, and Bergeron (2001) for lower mass WD ($< 1.10 M_{\odot}$), with Althaus et al. (2007) for massive WDs. M_i determined with Bressan et al. (2012).

- **NGC2516**: analysed in Cummings, Kalirai, Tremblay, and Ramirez-Ruiz (2016). The age of (150 ± 20) Myr was found with the PARSEC code (Bressan et al. (2012)). It has metallicity $[Fe/H] = 0.065$. t_{cool} and M_f were found with Fontaine, Brassard, and Bergeron (2001) for lower mass WD ($< 1.10 M_{\odot}$), with Althaus et al. (2007) for massive WDs. M_i determined with Bressan et al. (2012).

- **NGC3532**: analysed in Cummings, Kalirai, Tremblay, and Ramirez-Ruiz (2016) and Cummings, Kalirai, Tremblay, Ramirez-Ruiz, and Bergeron (2016). It has an age of (320 ± 20) Myr and $[Fe/H] = 0.09$. (Cummings, Kalirai, Tremblay, Ramirez-Ruiz, and Bergeron (2016)). The $t_{cluster}$ was calculated with the PARSEC code (Bressan et al. (2012)), the t_{cool} and the M_f with Fontaine, Brassard, and Bergeron (2001) for lower mass WD ($< 1.10 M_{\odot}$) and with Althaus et al. (2007) for massive WDs. M_i determined with Bressan et al. (2012).

- **PLEIADES**: analysed in Cummings, Kalirai, Tremblay, and Ramirez-Ruiz (2016) and Cummings, Kalirai, Tremblay, Ramirez-Ruiz, and Bergeron (2016). For this cluster we use an age of (135 ± 15) Myr and metallicity $[Fe/H] = 0.01$. The $t_{cluster}$ was calculated with the PARSEC code (Bressan et al. (2012)), the t_{cool} and the M_f with Fontaine, Brassard, and Bergeron (2001) for lower mass WD ($< 1.10 M_{\odot}$) and with Althaus et al. (2007) for massive WDs. M_i determined with Bressan et al. (2012).

- **NGC2168**: analysed in Cummings, Kalirai, Tremblay, and Ramirez-Ruiz (2016). The age of (170±20) Myr was found with the PARSEC code

(Bressan et al. (2012)). It has metallicity $[Fe/H] = -0.143$ (described in Kalirai, Fahlman, et al. (2003)). t_{cool} and M_f were found with Fontaine, Brassard, and Bergeron (2001) for lower mass WD ($< 1.10 M_\odot$), with Althaus et al. (2007) for massive WDs. M_i determined with Bressan et al. (2012).

- **SIRIUS B**: this is the only case of the considered WDs which does not belong to any cluster. It was included in Cummings, Kalirai, Tremblay, and Ramirez-Ruiz (2016) with an age of (237.5 ± 12.5) Myr and solar metallicity $[Fe/H] = 0.00$ (Liebert et al. (2005)). t_{cool} was found with Fontaine, Brassard, and Bergeron (2001). The initial mass M_i was calculated through the PARSEC code (Bressan et al. (2012)).

- **HYADES**: analysed in Kalirai, Marigo, and Tremblay (2014). The age is 625 Myr (Perryman et al. (1998)) and the metallicity $[Fe/H] = +0.12$. M_i follows from Bressan et al. (2012), M_f and t_{cool} from Bergeron, Saffer, and Liebert (1992) corrected with Tremblay and Bergeron (2009).

- **PRAESEPE**: very similar to the Hyades cluster, it was analysed in Kalirai, Marigo, and Tremblay (2014). The age is 625 Myr (Claver et al. (2001)) and the metallicity $[Fe/H] = +0.12$. M_i follows from Bressan et al. (2012), M_f and t_{cool} from Bergeron, Saffer, and Liebert (1992) corrected with Tremblay and Bergeron (2009).

In table 3.1 we expose the WDs belonging to the quoted clusters and their characteristics: the name ID, the remnant mass M_f and the extrapolated porgenitor mass, so that the mass of the star at the Zero Age Main Sequence M_i.

Table 3.1: White Dwarfs (WDs) included in this thesis. For each WD the name ID, the final mass M_f and the progenitor mass M_i are exposed.

CLUSTER	$[Fe/H]$	ID	M_f $[M_\odot]$	M_i $[M_\odot]$
NGC2099	+0.09	WD1	$0.48^{+0.09}_{-0.09}$	$2.79^{+0.05}_{-0.06}$
		WD3	$0.76^{0.13}_{-0.13}$	$2.92^{+0.16}_{-0.14}$
		WD4	$0.87^{+0.15}_{-0.15}$	$3.36^{+0.76}_{-0.40}$
		WD7	$0.88^{+0.19}_{-0.19}$	$3.26^{+0.78}_{-0.40}$
		WD11	$0.96^{+0.06}_{-0.06}$	$2.86^{+0.07}_{-0.07}$
		WD12	$0.55^{+0.07}_{-0.07}$	$3.30^{+0.30}_{-0.22}$
		WD14	$0.45^{+0.08}_{-0.08}$	$3.31^{+0.26}_{-0.20}$
		WD18	$0.76^{+0.036}_{-0.036}$	$3.00^{+0.03}_{-0.02}$
		WD2	$0.77^{+0.045}_{-0.045}$	$3.09^{+0.04}_{-0.03}$

to be continued

continued

CLUSTER	$[Fe/H]$	ID	M_f $[M_\odot]$	M_i $[M_\odot]$
		WD24	$0.80^{+0.068}_{-0.068}$	$3.32^{+0.15}_{-0.10}$
		WD6	$0.89^{+0.069}_{-0.069}$	$3.96^{+0.66}_{-0.35}$
		WD21	$0.85^{+0.069}_{-0.069}$	$3.72^{+0.39}_{-0.23}$
		WD5	$0.74^{+0.062}_{-0.062}$	$3.30^{+0.13}_{-0.09}$
		WD10	$0.71^{+0.054}_{-0.054}$	$3.15^{+0.07}_{-0.06}$
		WD16	$0.87^{+0.095}_{-0.095}$	$3.78^{+0.72}_{-0.33}$
		WD17	$0.96^{+0.099}_{-0.099}$	$4.05^{+1.54}_{-0.52}$
		WD13	$0.91^{+0.082}_{-0.082}$	$3.42^{+0.24}_{-0.16}$
		WD9	$0.59^{+0.078}_{-0.078}$	$3.25^{+0.16}_{-0.11}$
		WD25	$0.70^{+0.03}_{-0.03}$	$2.95^{+0.10}_{-0.10}$
		WD28	$0.75^{+0.03}_{-0.03}$	$3.07^{+0.13}_{-0.11}$
		WD33	$1.28^{+0.05}_{-0.05}$	$3.58^{+0.62}_{-0.41}$
NGC6791	+0.37	WD7	$0.53^{+0.02}_{-0.02}$	$1.16^{+0.04}_{-0.41}$
NGC6121	−1.10	WD00	$0.52^{+0.04}_{-0.04}$	$0.80^{+0.05}_{-0.05}$
		WD04	$0.50^{+0.03}_{-0.03}$	$0.80^{+0.05}_{-0.05}$
		WD06	$0.59^{+0.04}_{-0.04}$	$0.80^{+0.05}_{-0.05}$
		WD15	$0.55^{+0.04}_{-0.04}$	$0.80^{+0.05}_{-0.05}$
		WD20	$0.51^{+0.05}_{-0.05}$	$0.80^{+0.05}_{-0.05}$
		WD24	$0.51^{+0.03}_{-0.03}$	$0.80^{+0.05}_{-0.05}$
		WD02	$0.75^{+0.03}_{-0.03}$	$0.80^{+0.05}_{-0.05}$
		WD05	$0.48^{+0.03}_{-0.03}$	$0.80^{+0.05}_{-0.05}$
		WD09	$0.79^{+0.05}_{-0.05}$	$0.80^{+0.05}_{-0.05}$
		WD29	$0.41^{+0.04}_{-0.04}$	$0.80^{+0.05}_{-0.05}$
NGC6819	+0.049	WD6	$0.56^{+0.02}_{-0.02}$	$1.60^{+0.06}_{-0.05}$
		WD7	$0.59^{+0.02}_{-0.02}$	$1.62^{+0.07}_{-0.05}$
NGC7789	−0.035	WD4 c	$0.56^{+0.02}_{-0.02}$	$2.08^{+0.08}_{-0.08}$
		WD5	$0.64^{+0.03}_{-0.03}$	$2.02^{+0.07}_{-0.14}$
		WD6c	$0.72^{+0.03}_{-0.03}$	$2.10^{+0.09}_{-0.09}$
		WD8	$0.66^{+0.04}_{-0.04}$	$2.02^{+0.09}_{-0.11}$
NGC2323	0.00	WD10	$1.068^{+0.045}_{-0.045}$	$4.69^{+0.01}_{-0.01}$
		WD11	$1.075^{+0.032}_{-0.032}$	$4.69^{+0.01}_{-0.01}$
NGC2287	0.00	WD2	$0.909^{+0.028}_{-0.028}$	$4.81^{+0.16}_{-0.12}$
		WD4	$1.065^{+0.027}_{-0.027}$	$5.93^{+0.52}_{-0.38}$
		WD5	$0.901^{+0.028}_{-0.028}$	$4.83^{+0.16}_{-0.12}$
NGC2516	+0.065	WD1	$0.925^{+0.027}_{-0.027}$	$5.19^{+0.14}_{-0.12}$
		WD2	$0.981^{+0.040}_{-0.040}$	$4.88^{+0.13}_{-0.10}$
		WD3	$0.918^{+0.027}_{-0.027}$	$5.31^{+0.19}_{-0.14}$
		WD5	$0.970^{+0.027}_{-0.027}$	$5.12^{+0.13}_{-0.11}$
NGC3532	+0.09	WD1	$0.950^{+0.026}_{-0.026}$	$4.13^{+0.11}_{-0.09}$

to be continued

continued

CLUSTER	$[Fe/H]$	ID	M_f $[M_\odot]$	M_i $[M_\odot]$
		WD5	$0.804^{+0.028}_{-0.028}$	$3.55^{+0.03}_{-0.03}$
		WD9	$0.752^{+0.026}_{-0.026}$	$3.46^{+0.01}_{-0.01}$
		WD1 0	$0.838^{+0.027}_{-0.027}$	$3.64^{+0.04}_{-0.04}$
		J110659	$0.922^{+0.031}_{-0.031}$	$4.41^{+0.21}_{-0.17}$
		J110658	$0.945^{+0.029}_{-0.029}$	$4.83^{+0.37}_{-0.26}$
		J110758	$0.990^{+0.028}_{-0.028}$	$5.07^{+0.49}_{-0.34}$
		J11035837	$1.11^{+0.03}_{-0.03}$	$5.40^{+1.36}_{-0.55}$
Pleiades	+0.01	LB1497	$1.046^{+0.028}_{-0.028}$	$6.85^{+0.57}_{-0.41}$
		GD50	$1.26^{+0.02}_{-0.02}$	$6.41^{+0.72}_{-0.41}$
		PG0136	$1.20^{+0.03}_{-0.03}$	$5.78^{+0.48}_{-0.32}$
NGC2168	−0.143	LAWDS1	$0.911^{+0.039}_{-0.039}$	$4.48^{+0.09}_{-0.06}$
		LAWDS2	$0.940^{+0.061}_{-0.061}$	$4.55^{+0.18}_{-0.12}$
		LAWDS5	$0.801^{+0.031}_{-0.031}$	$4.28^{+0.01}_{-0.01}$
		LAWDS6	$0.731^{+0.029}_{-0.029}$	$4.28^{+0.01}_{-0.01}$
		LAWDS12	$1.009^{+0.037}_{-0.037}$	$4.69^{+0.13}_{-0.11}$
		LAWDS14	$0.988^{+0.038}_{-0.038}$	$4.98^{+0.21}_{-0.17}$
		LAWDS15	$1.009^{+0.032}_{-0.032}$	$5.16^{+0.22}_{-0.18}$
		LAWDS22	$0.807^{+0.035}_{-0.035}$	$4.28^{+0.01}_{-0.01}$
		LAWDS27	$1.071^{+0.031}_{-0.031}$	$5.49^{+0.35}_{-0.27}$
		LAWDS29	$0.984^{+0.034}_{-0.034}$	$4.67^{+0.12}_{-0.10}$
		LAWDS30	$0.878^{+0.048}_{-0.048}$	$4.65^{+0.16}_{-0.12}$
	0.00	Sirius B	$0.982^{+0.024}_{-0.024}$	$4.69^{+0.15}_{-0.12}$
Hyades	+0.12	0352069	$0.80^{+0.03}_{-0.03}$	$3.59^{+0.21}_{-0.15}$
		0406169	$0.85^{+0.03}_{-0.03}$	$3.49^{+0.13}_{-0.10}$
		0421162	$0.70^{+0.03}_{-0.03}$	$2.90^{+0.02}_{-0.02}$
		0425168	$0.71^{+0.03}_{-0.03}$	$2.79^{+0.01}_{-0.01}$
		0431126	$0.69^{+0.03}_{-0.03}$	$2.84^{+0.02}_{-0.02}$
		0437138	$0.74^{+0.06}_{-0.06}$	$3.41^{+0.21}_{-0.15}$
		0438108	$0.73^{+0.03}_{-0.03}$	$2.78^{+0.01}_{-0.01}$
		0348339	$0.80^{+0.03}_{-0.03}$	$3.55^{+0.19}_{-0.14}$
		HS0400	$0.76^{+0.01}_{-0.01}$	$3.49^{+0.03}_{-0.03}$
		0625415	$0.66^{+0.03}_{-0.03}$	$2.97^{+0.03}_{-0.03}$
		0637477	$0.80^{+0.04}_{-0.04}$	$3.59^{+0.26}_{-0.18}$
Praesepe	+0.12	0833194	$0.79^{+0.04}_{-0.04}$	$3.41^{+0.16}_{-0.16}$
		0836199	$0.82^{+0.04}_{-0.04}$	$3.59^{+0.18}_{-0.13}$
		0837185	$0.87^{+0.04}_{-0.04}$	$3.66^{+0.21}_{-0.16}$
		0837199	$0.80^{+0.04}_{-0.04}$	$3.13^{+0.06}_{-0.05}$
		0840190	$0.91^{+0.05}_{-0.05}$	$3.97^{+0.40}_{-0.24}$
		0840200	$0.79^{+0.04}_{-0.04}$	$3.39^{+0.12}_{-0.09}$
		0843184	$0.89^{+0.05}_{-0.05}$	$3.77^{+0.27}_{-0.18}$

As said before, although the information comes from one group of research, the consistency can not yet be considered fully achieved. Therefore, to improve our analysis we choose to use the semi-empirical data provided by the prof. Jeffrey D. Cummings (private communication) who analysed the spectra of the WDs in table 3.1 on page 21 with the same method.

This choice significantly enhances the validity of the analysis: in figure 3.2 we show the semi-empirical data from prof. Jeffrey D. Cummings. We immediately note that the dispersion decreases considerably, above all at $M_i = 1M_\odot$ and $3M_\odot \leq M_i \leq 5M_\odot$. An interesting sharp maximum occurs at $M_i = 2M_\odot$ and a flattening takes place at $M_i \simeq 4M_\odot$. To test the models in the section 4.3 on page 47 we use the quantities provided by prof. Jeffrey D. Cummings.

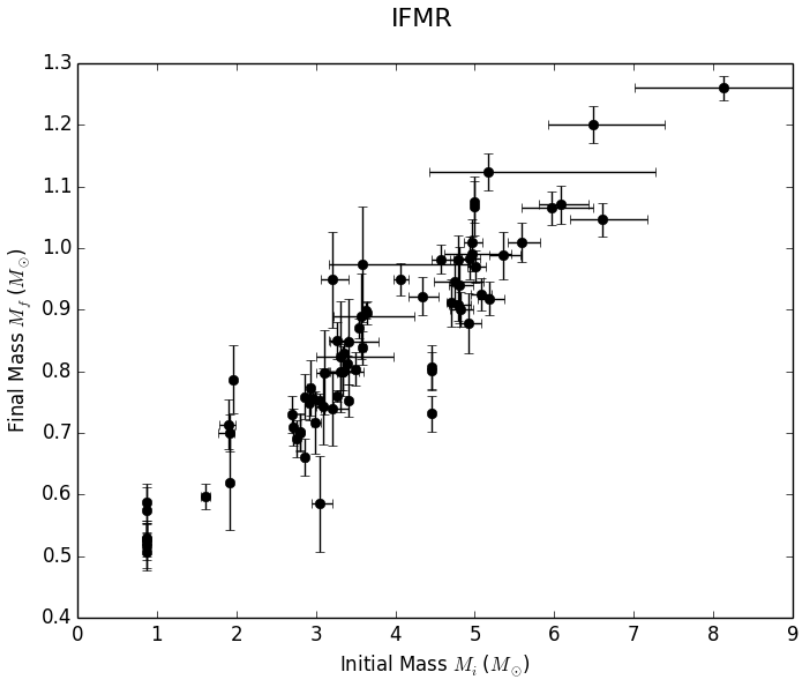

Figure 3.2: Semi-empirical data provided by the prof. Jeffrey D. Cummings (private communication).

Chapter 4

Predicted Initial-Final Mass Relation

In this section we analyse the predicted dependencies of the IFMR and four theoretical models for the stellar evolution, from the ZAMS to the post-AGB phase. As said before, among various physical processes that can affect the AGB evolution, the main factors that must be considered are the *metallicity*, the 2^{nd} *dredge-up* on the E-AGB, the 3^{rd} *dredge-up* and the *mass loss* on the TP-AGB. Even if it is difficult to disentangle the effects of each process involved, we can derive some general trends.

4.1 The effect of the 2^{nd} dredge-up on the E-AGB

During the Early AGB (E-AGB) phase, the base of the convective envelope moves inwards causing a mixing of H-burnt material to the surface (see section 2.1.1 on page 10). This process, termed 2^{nd} dredge-up, occurs only for stars with $M_i \geq 3 - 4M_{\odot}$. The effects of the 2^{nd} dredge-up on the core growth are exposed in figure 4.1 on the following page from Marigo (2013): the left panel shows the predicted core mass as a function of the stellar initial mass, according to different authors and metallicities, at the onset of the E-AGB phase as if the 2^{nd} dredge-up would never take place, while the right panel shows the significant change in slope which occurs at $3M_{\odot}$ if the 2^{nd} dredge-up is included. Hence, the change of slope observed in figure 3.2 on the preceding page can be a hint of the occurrence of the 2nd dredge-up during the E-AGB; thus, if true, the IFMR could provide a direct observation of this effect.

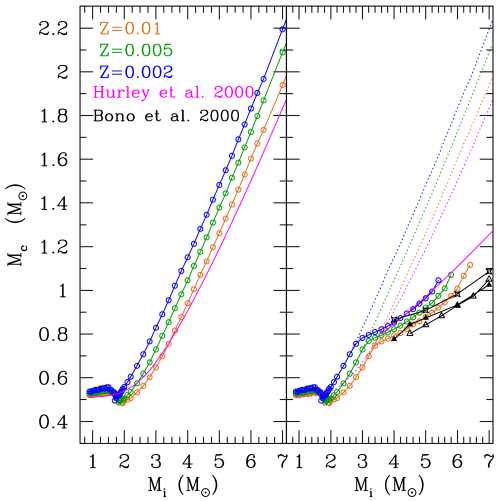

Figure 4.1: Effects of the 2^{nd} dredge-up according to different authors. Circles correspond to computation of the Padova stellar code (Bressan et al. (2012)) for different metallicities. Figure from Marigo (2013).

4.2 Key processes on TP-AGB

In order to investigate the effects of the key processes that characterize the TP-AGB phase, we rely on four different sets of stellar model, namely:

- The F.R.U.I.T.Y. database by Cristallo, Straniero, Piersanti, et al. (2015), Cristallo, Piersanti, et al. (2011) and Cristallo, Straniero, Gallino, et al. (2009), computed by means of the FRANEC Code (Chieffi, Limongi, and Straniero (1998)). In this model solar distribution presented in Lodders (2003) and opacity by Lederer and Aringer (2009) are adopted. The pre-AGB mass loss rate is calculated with the Reimers' formula with an assumed $\eta_R = 0.4$, while the AGB mass loss rate is empirically calibrated on the observed period-luminosity relation, a procedure similar to Vassiliadis and Wood (1993). The free parameter of the mixing length theory of convection is set to $\alpha = 2.15$. It is important to stress that no convective core overshoot is assumed during core H-burning, while semi-convection is applied during core He-burning.

- The second model discussed is presented in A. I. Karakas (2010) and references therein. The solar composition and the initial abundances are taken from Anders and Grevesse (1989). They employ the mixing length theory with $\alpha = 1.75$. The mass loss rate is calculated both with Vassiliadis and Wood (1993) and Reimers' formula (for metallicity

$Z = 0.02$, $\eta_R = 3.5$). The opacity adopted depends significantly by the atmosphere temperature: for high T they assume OPAL opacities from Iglesias and Rogers (1996); for models from A. Karakas and Lattanzio (2007) they use Bessell et al. (1989) corrected by Chiosi, Wood, and Capitanio (1993); for low T Ferguson et al. (2005). No convective overshoot is assumed.

- The third model is provided by Weiss and Ferguson (2009). It is computed by the Garching Stellar Evolution Code (GARSTEC), and it assumes a solar mixture from Seaton et al. (1992), a mixing length theory parameter $\alpha = 1.75$ and a treatment for the opacities structured taking into account the temperature of the atmosphere: for high T they use OPAL tables from Iglesias and Rogers (1996); for low T Ferguson et al. (2005). For the C-enriched mixture they use Marigo (2002). The mass loss rate adopted depends on the evolution phase: for the Red Giant Branch phase (RGB) they develop the Reimers' formula with a $\eta_R = 1$ for $M_{ZAMS} \geq 1.7$ and $\eta_R = 0.4$ for $M_{ZAMS} \leq 1.7$; instead, for the AGB phase they stress the effects of the composition adopting a Wachter et al. (2002) for Carbon stars and van Loon et al. (2005) for Oxygen ones. Finally, it is important to note that convective overshoot is implemented in their treatment, according to Schwarzschild criterion ($f = 0.016$ assumed).

- The last prescription is calculated with the `COLIBRI` codes from Marigo, Bressan, et al. (2013), from the first thermal pulse up to the almost complete ejection of the envelope. Stellar convection is described by means of the classical mixing length theory. The mixing length $l_{\rm conv}$ is assumed to scale linearly with the pressure scale height, $H_{\rm p}$, according to setting the proportionality factor $\alpha_{\rm MLT} = 1.74$, following their recent calibration of the solar model (Bressan et al. (2012)). Overshoot is applied to the borders of convective cores as well as at the base of the convective envelope, and is described through the parameter Λ which sets its extension in units of $H_{\rm p}$. In the range of intermediate stellar masses under consideration their default choice is $\Lambda_{\rm c} = 0.5$ for convective core overshoot (across the border) and $\Lambda_{\rm e} = 0.7$ for envelope overshoot.

  The network of nuclear reaction rates includes the proton-proton chains, the CNO tri-cycle, the Ne-Na and Mg-Al cycles, and the most important α-capture reactions, together with few α-n reactions. In total they consider 42 reactions rates (for the complete list and references see table 1 in Marigo, Bressan, et al. (2013).

The initial distribution of metals is assumed to follow a scaled-solar pattern Caffau et al. (2011), which corresponds to a present-day Sun's metallicity $Z_{\odot} = 0.01524$.

To compute the mass-loss rate they first adopt the prescriptions for cold-chromospheric mass loss presented in Cranmer and Saar (2011) and then, as the star enters the dust-driven wind regime, they adopt the relation from Bloecker (1995) for M-type stars (with surface C/O<1) and the results from Mattsson, Wahlin, and Höfner (2010) based on dynamical atmospheres for C-stars (with surface C/O>1). These mass-loss relations are found to give a good reproduction of AGB stars counts in the Magellanic Clouds. In `COLIBRI` they account for the changes in the surface chemical composition caused by the occurrence of the third dredge-up and hot-bottom burning. As for the third dredge-up they adopt a semi-numerical approach. The authors perform envelope integrations at the stage of the post-flash luminosity peak to determine if and when it is expected to take place according to a temperature criterion.

The chemical composition of the pulse-driven convection zone is predicted by solving a nuclear network that includes the main α-capture reactions. The efficiency λ of the third dredge-up as a function of stellar mass and metalicity is computed with an analytic formalism based on full stellar models (A. I. Karakas, Lattanzio, and Pols (2002)), but imposing that $\lambda \leq 0.5$ at any stellar mass. It includes adjustable parameters which are suitably modified in order to reproduce basic observables of AGB stars, such as carbon star luminosity functions, M-C transition luminosities, surface C/O ratios (e.g. Marigo (2015), Rosenfield et al. (2014) and Marigo and Girardi (2007).

The process of hot-bottom burning experienced by massive AGB stars (with initial masses $M_{\rm i} \geq 3-4\,M_{\odot}$, depending on metallicity and model details) is consistently taken into account in terms of energetics and nucleosynthesis. The nucleosynthesis of all species is coupled in time and in space with a diffusive description of convection. A key characteristic of the `COLIBRI` code is that the equation of state for $\simeq 800$ atomic and molecular species, and the Rosseland mean of the gas opacities across the atmosphere and the deep envelope are computed on-the-fly, ensuring a full consistency with the changing abundances of all involved chemical elements (Marigo and Aringer (2009)).

Table 4.1: Predicted final masses provided by Cristallo, Straniero, Piersanti, et al. (2015).

M_i	M_f					
	0.02	0.014	0.010	0.008	0.003	0.001
1.30	0.6227	0.6341	0.6276	0.6326	0.6409	0.6437
1.50	0.6316	0.6324	0.6163	0.6375	0.6417	0.6482
2.00	0.6293	0.6322	0.6303	0.6354	0.6415	0.6611
2.50	0.6396	0.6410	0.6392	0.6399	0.6572	0.7024
3.00	0.6493	0.6571	0.6610	0.6736	0.7464	0.7921
4.00	0.7540	0.8054	0.8166	0.8300	0.8571	0.8717
5.00	0.8462	0.8682	0.8764	0.8776	0.9238	0.9394
6.00	0.9150	0.9409	0.9378	0.9553	1.020	1.044

Table 4.2: Predicted final masses provided by A. I. Karakas (2010).

M_i	M_f			
	0.02	0.008	0.004	0.0001
1.00	0.564	0.654	0.611	-
1.25	0.574	0.600	0.634	0.664
1.50	0.593	0.626	0.616	-
1.75	0.615	0.636	0.631	0.664
1.90	0.630	0.640	0.639	-
2.00	0.639	-	-	0.685
2.10	-	0.645	0.650	-
2.25	0.661	0.653	0.662	0.711
2.50	0.658	0.666	0.676	0.735
3.00	0.680	0.700	0.730	0.819
3.50	0.715	0.769	0.820	0.849
4.00	0.793	0.841	0.856	0.873
4.50	0.852	0.861	0.872	-
5.00	0.874	0.886	0.908	0.936
5.50	0.900	0.907	0.932	-
6.00	0.929	0.947	0.978	1.006
6.50	0.963	-	-	-

Table 4.3: Predicted final masses provided by Weiss and Ferguson (2009).

M_i	M_f				
	0.04	0.02	0.008	0.004	0.0005
1.0	0.510	0.508	0.531	0.531	0.537
1.2	0.521	0.524	0.531	0.536	0.550
1.5	0.531	0.539	0.537	0.537	0.578
1.6	0.536	0.538	0.537	0.536	0.578
1.8	0.537	0.524	0.526	0.493	0.564
2.0	0.552	0.543	0.528	0.528	0.599
2.6	0.587	0.560	0.576	0.653	0.734
3.0	0.628	0.617	0.686	0.746	0.772
4.0	0.751	0.783	0.816	0.818	0.829
5.0	0.829	0.850	0.879	0.898	-
6.0	0.908	0.937	0.993	1.047	-

Table 4.4: Predicted final masses provided by Marigo, Bressan, et al. (2013).

M_i	M_f					
	0.02	0.014	0.008	0.004	0.001	0.0005
1.000	0.5396	0.5374	0.5374	0.5401	0.5458	0.5454
1.050	0.5475	0.5447	0.5445	0.5444	0.5486	0.5504
1.100	0.5559	0.5527	0.5494	0.5501	0.5558	0.5566
1.150	0.5649	0.5605	0.5560	0.5565	0.5606	0.5614
1.200	0.5748	0.5683	0.5642	0.5626	0.5647	0.5667
1.250	0.5825	0.5775	0.5724	0.5685	0.5710	0.5742
1.300	0.5904	0.5869	0.5803	0.5753	0.5786	0.5801
1.350	0.5978	0.5955	0.5877	0.5836	0.5842	0.5849
1.400	0.6054	0.6032	0.5951	0.5884	0.5917	0.5938
1.450	0.6126	0.6106	0.6014	0.5949	0.5941	0.5959
1.500	0.6197	0.6182	0.6096	0.5990	0.5948	0.6001
1.550	0.6268	0.6254	0.6144	0.6032	0.5973	0.6007
1.600	0.6322	0.6310	0.6181	0.6070	0.5955	0.5821
1.650	0.6378	0.6385	0.6232	0.6104	0.5857	0.5909
1.700	0.6433	0.6415	0.6250	0.6152	0.6034	0.6162
1.750	0.6502	0.6454	0.6298	0.6121	0.6115	0.6231
1.800	0.6554	0.6498	0.6315	0.6202	0.6218	0.6312
1.850	0.6616	0.6489	0.6369	0.6253	0.6420	0.6446
1.900	0.6681	0.6524	0.6401	0.6338	0.6515	0.6578
1.950	0.6732	0.6548	0.6441	0.6379	0.6654	0.6676
2.000	0.6753	0.6584	0.6478	0.6443	0.6688	0.6813
2.050	0.6789	0.6589	0.6524	0.6529	0.6836	0.6901
2.100	0.6796	0.6641	0.6548	0.6579	0.6914	0.7004
2.150	0.6818	0.6655	0.6605	0.6628	0.7002	0.7128

to be continued

continued

M_i	M_f					
	0.02	0.014	0.008	0.004	0.001	0.0005
2.200	0.6834	0.6680	0.6665	0.6703	0.7107	0.7213
2.250	0.6857	0.6751	0.6675	0.6771	0.7208	0.7325
2.300	0.6879	0.6759	0.6745	0.6857	0.7318	0.7396
2.400	0.6931	0.6838	0.6875	0.7009	0.7500	0.7634
2.600	0.7079	0.7054	0.7113	0.7353	0.7861	0.7973
2.800	0.7266	0.7280	0.7384	0.7740	0.8138	0.8205
3.000	0.7487	0.7517	0.7681	0.8037	0.8298	0.8377
3.200	0.7734	0.7779	0.7985	0.8215	0.8457	0.8504
3.400	0.7928	0.8029	0.8197	0.8382	0.8619	0.8649
3.600	0.8143	0.8215	0.8351	0.8520	0.8766	0.8778
3.800	0.8274	0.8357	0.8507	0.8683	0.8892	0.8917
4.000	0.8422	0.8501	0.8679	0.8845	0.9068	0.9065
4.200	0.8555	0.8656	0.8817	0.8986	0.9186	0.9224
4.400	0.8731	0.8814	0.8968	0.9137	0.9371	0.9394
4.800	0.9007	0.9081	0.9235	0.9466	0.9787	0.9841
5.000	0.9119	0.9219	0.9395	0.9682	1.0051	1.0102
5.200	0.9249	0.9370	0.9585	0.9923	-	-
5.400	0.9402	0.9527	0.9817	1.0145	-	-
5.600	0.9561	0.9723	1.0044	-	-	-
5.800	0.9772	0.9940	-	-	-	-
6.000	1.0002	1.0222	-	-	-	-

4.2.1 Dependence on the 3rd dredge-up

As explained in 2.1.2 on page 10, during a thermal pulse an intershell convective region develops, mixing the intershell material with the products of the He-burning. Meanwhile, the outer envelope is still convective due to the preceding expansion phase. Subsequently, the He-shell dies down, driving with its energy release an expansion which leads to a deeper penetration of the convective outer envelope. It is important to note that the intershell convective zone only occurs during the pulse. Thus, for stars with $M_{initial} \geq 2M_{\odot}$ the convective layers and the extinct intershell convective zone overlap. This process leads to a partially mixing of He-burnt material to the surface, called the 3^{rd} dredge-up, which has two important consequences:

- it contributes to stellar nucleosynthesis;
- it limits the growth of the Carbon-Oxygen core.

In this thesis we focus only on the second consequence. As said in section 2.1.2 on page 10, the efficiency of the 3^{rd} dredge-up is calculated

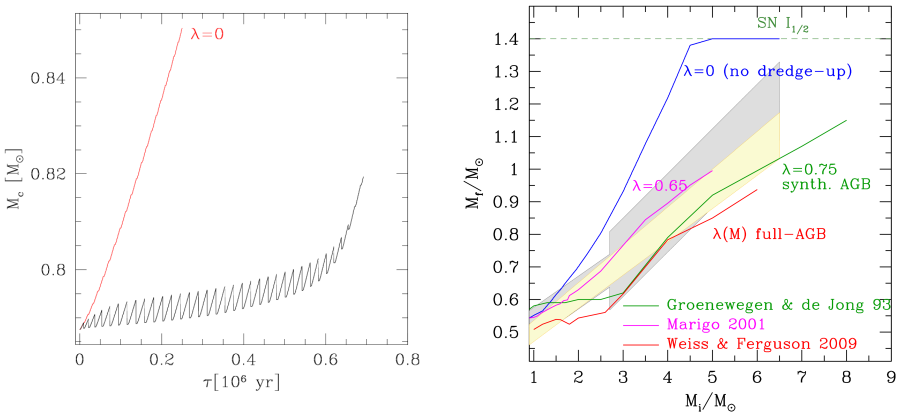

(a) (b)

Figure 4.2: Figure (a): predicted core mass growth during the TP-AGB phase for a $M_i = 4M_\odot$ and $Z = 0.014$ star. The red line shows the core growth if $\lambda = 0$, the black line correspond to $\lambda \neq 0$. From Marigo, Bressan, et al. (2013). Figure (b): dependence of the predicted IFMR from the efficiency of the third dredge-up (from Marigo (2013)).

through the λ parameter (formula 2.1 on page 11). A $\lambda = 0$ corresponds to an absence of dredge-up, and a $\lambda = 1$ means that all the material that the core accretes during the interpulse period is brought away after the dredge-up. In figure 4.2 (left panel) the predicted effects of the 3^{rd} dredge-up on the core mass growth during the TP-AGB phase are exposed for a $M_i = 4M_\odot$ and $Z = 0.014$ star (model from Marigo, Bressan, et al. (2013)). We can note the saw-tooth trend for the $\lambda \neq 0$ line (black line) due to the occurence of the dredge-up events. Furthermore, as exposed in Marigo (2013), by assuming no dredge-up the intermediate mass stars would be able to reach the Chandrasekhar limit and explode as SN $I_{1/2}$ (figure 4.2, right panel). However, the semi-empirical IFMR indicates that stars with $M_i \simeq 5 - 7M_\odot$ produce WD with final mass $M_f \simeq 1M_\odot$.

The λ value is still affected by large uncertainties due to the lack of a complete convection theory. Actually, to estimate and put constraints on the λ parameter the observed data must be used. It follows that its value changes significantly using different models. We stress this trend analysing the sup-solar metallicity $Z = 0.02$ in figure 4.3 on the next page for two models: according to Cristallo, Straniero, Piersanti, et al. (2015), the efficiency increases up to $\simeq 0.6$ which occurs at $M_i = 3M_\odot$, then it decreases to $\simeq 0.3$ at $M_i = 6M_\odot$; instead, according to A. I. Karakas (2010) the 3^{rd} dredge-up at this metallicity takes place only for star with $M_i > 2M_\odot$, but the efficiency is

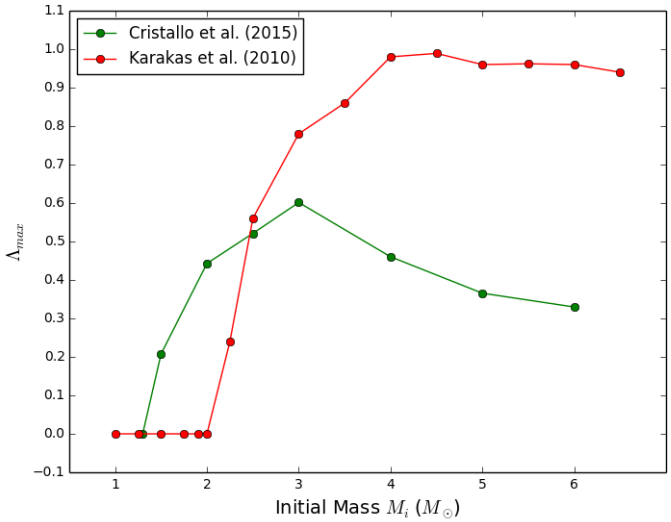

Figure 4.3: λ_{max} dependence on the initial mass M_i according to Cristallo, Straniero, Piersanti, et al. (2015) (green line) and to A. I. Karakas (2010) (red line) for $Z = 0.02$.

significantly larger, reaching $\lambda = 0.99$ at $M_i = 4.50 M_\odot$. Hence, the remnant mass will practically coincide with the core mass after the 2^{nd} dredge-up.

We expose the values of the efficiency and the dredged-up mass $\Delta M_{dredge-up}$ for sup-solar metallicity $Z = 0.02$ in tables 4.6 on page 40, 4.8 on page 41 and 4.9 on page 41.

The core growth during the AGB phase is exposed in figure 4.4 on the next page. All the proceedings show an initial increasing trend up to the peak, followed by a decrease and finally a plateau: according to Cristallo, Straniero, Piersanti, et al. (2015) (blue line) the peak of $\simeq 0.12 M_\odot$ is at $M_i = 2.5 M_\odot$; for Weiss and Ferguson (2009) (yellow line) the maximum value of $0.065 M_\odot$ occurs for $M_i = 2 M_\odot$; A. I. Karakas (2010) (red line) predict a peak of $0.124 M_\odot$ at $M_i = 2.5 M_\odot$; according to Marigo, Bressan, et al. (2013) (green line), the slope is so steep that the peak of $0.18 M_\odot$ occurs at $M_i \simeq 2 M_\odot$ and the plateau ($3.6 M_\odot \leq M_i \leq 4.8 M_\odot$) is followed by a further decrease.

The fundamental effects of the 3^{rd} dredge-up and the core mass growth are also displayed in figure 4.5 on page 35. The dashed lines represent the final mass as if the 3^{rd} dredge-up would never occur. It is interesting to note that according to Cristallo, Straniero, Piersanti, et al. (2015) the 3^{rd} dredge-up occurs immediately, while according to A. I. Karakas (2010) and Marigo, Bressan, et al. (2013) it takes place only for $M_i \geq 2 - 2.2 M_\odot$. The predicted

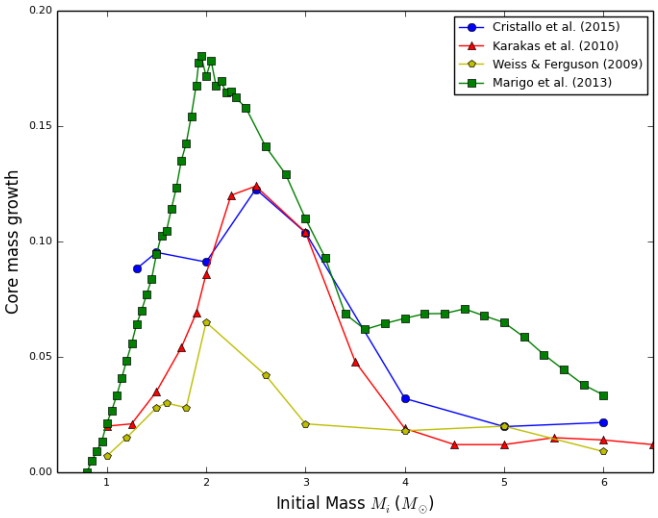

Figure 4.4: Core mass growth according to the models analysed: Cristallo, Straniero, Piersanti, et al. (2015) (blue line), A. I. Karakas (2010) (red line), Weiss and Ferguson (2009) (yellow line) and Marigo, Bressan, et al. (2013) (green line) for metallicity Z=0.02.

trends for the core mass at the first thermal pulse $M_{c,1TP}$ are quite similar, showing a minimum at $2M_\odot$ (Weiss and Ferguson (2009) and Marigo, Bressan, et al. (2013)) if the convective overshooting is assumed, at $2.5M_\odot$ (Cristallo, Straniero, Piersanti, et al. (2015) and A. I. Karakas (2010)) if it is not. This minimum, which corresponds to the maximum value of the core growth in figure 4.4, reflects the transition from stars that ignite He in a degenerate way, which trigger the He-burning when the core has mass $\sim 0.45M_\odot$, to stars that avoid the degeneracy, which start He-burning with a $\sim 0.35M_\odot$ core mass: indeed, during the core contraction in the H-burning shell phase, for $M_i \leq 2 - 2.5M_\odot$ stars the energy released is stolen by the electrons in order to fill their lowest energy state up to the Fermi level, hence the temperature increases more slowly and the core can accrete more material. This minimum lasts until the first thermal pulse and then, during the TP-AGB phase, it disappears.

Finally, to mathematically quantify the percentage of material that undergoes mixing process instead of accrete the core we introduce the rate:

$$\frac{\sum_{i,p=1}^{N} \Delta M_{dredge-up,i}}{M_f - M_{c,1TP} + \sum_{i,p=1}^{N} \Delta M_{dredge-up,i}} \tag{4.1}$$

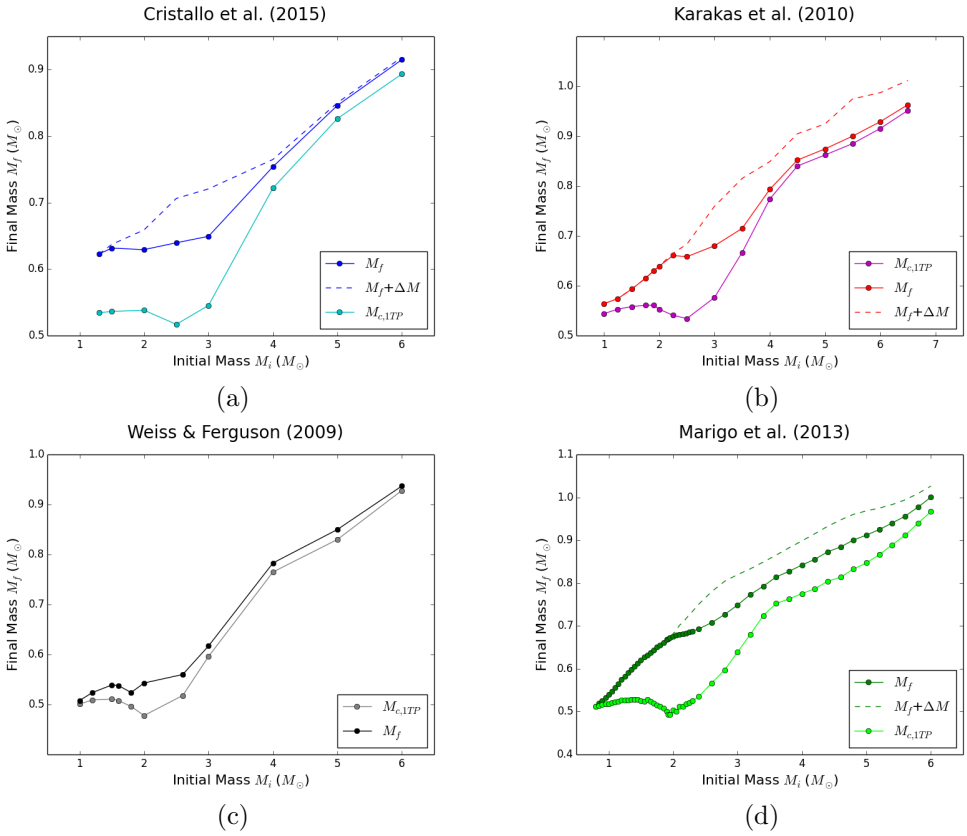

Figure 4.5: Figure (a): IFMR predicted by Cristallo, Straniero, Piersanti, et al. (2015) for $Z = 0.02$. Figure (b): IFMR predicted by A. I. Karakas (2010) for $Z = 0.02$. Figure (c): IFMR predicted by Weiss and Ferguson (2009) for $Z = 0.02$. Figure (d): IFMR predicted by Marigo, Bressan, et al. (2013) for $Z = 0.02$.

for the initial mass M_i. The term $\sum_{i,p=1}^{N} \Delta M_{dredge-up,i}$ is the sum of the N thermal pulses which take place during the TP-AGB phase (where N number depending on M_i). The results are exposed in table 4.5. According to the values proposed for λ, the material subtracted to the core mass growth has a peak of about 41% at $M_i = 3M_\odot$ for Cristallo, Straniero, Piersanti, et al. (2015), 83% at $M_i = 5.50M_\odot$ for A. I. Karakas (2010), 47% at $M_i = 4.60M_\odot$ for Marigo, Bressan, et al. (2013)

Table 4.5: Material subtracted to the core mass growth calculated with the formula 4.1 on page 34 for $Z = 0.02$

Author	M_i $[M_\odot]$	Material subtracted to the core mass growth (%)
Cristallo et al. (2015)	1.3	0.0
	1.5	5.5
	2	24.5
	2.5	35.2
	3	40.7
	4	25.5
	5	17.0
	6	14.4
Karakas et al. (2010)	1.0	0.00
	1.25	0.00
	1.50	0.00
	1.75	0.00
	1.90	0.00
	2.00	0.00
	2.25	3.78
	2.50	16.81
	3.00	43.25
	3.50	67.63
	4.00	74.54
	4.50	81.45
	5.00	80.66
	5.50	83.28
	6.00	80.59
	6.50	80.23
Marigo et al. (2013)	2.00	3.67
	2.05	6.12
	2.10	11.59
	2.15	13.38
	2.20	16.86
	2.25	19.51
	2.30	21.98
	2.40	26.82

to be continued

continued

Author	M_i $[M_\odot]$	Material subtracted to the core mass growth (%)
	2.60	33.86
	2.80	37.52
	3.00	39.25
	3.20	39.20
	3.40	45.09
	3.60	45.15
	3.80	45.97
	4.00	45.76
	4.20	46.51
	4.40	46.35
	4.60	47.13
	4.80	46.85
	5.00	46.53
	5.20	46.10
	5.40	45.76
	5.60	46.12
	5.80	45.59
	6.00	43.78

4.2.2 Dependence on mass loss

As explained in section 2.2 on page 12, the mass loss drives the TP-AGB phase itself: the more efficient is the process, the shorter will be the phase. Therefore, a shorter phase limits the growth of the core. It is important to stress that, even if the majority of the mass loss takes place during the AGB and the planetary nebula phases, the ejection of material occurs also during the Red Giant Branch phase. Although the process is not well understood, it seems to be sensitive to stellar metallicity (Kalirai, Bergeron, et al. (2007)).

Over the years, many functions were proposed to describe this complicated process, such as the Reimers' formula (1975), Vassiliadis and Wood (1993) and more recently Wachter et al. (2002) and van Loon et al. (2005). In tables 4.6 on page 40, 4.7 on page 40, 4.8 on page 41 and 4.9 on page 41 the mass loss functions used by each model are shown.

The influence of stellar winds in driving the core mass growth was deeply investigated by Kalirai, Marigo, and Tremblay (2014). In this thesis we assume the conclusions of the latter paper, of which we report the main results for $Z = 0.02$. They compared five predicted models:

- The classical Reimers' formula (1975): although it is inadeguated to describe the mass loss rate during the TP-AGB phase, it is still an

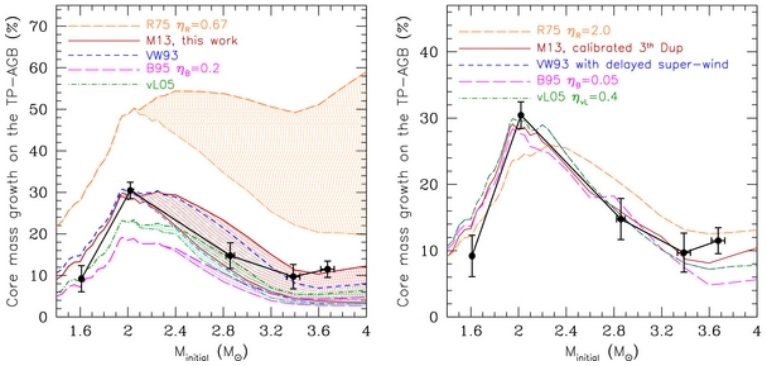

Figure 4.6: The Reimers' law (orange curves); Marigo's prescription (red curves); Vassiliadis and Wood (blue curves); Blöcker (magenta curves); van Loon (green curves).The left panel shows the effects of varyng the λ efficiency (the hatched region). In the right panel the improved parameters allow a better agreement between empirical data and predicted proceedings. Figure from Kalirai, Marigo, and Tremblay (2014)

important reference for the metallicity dependence and, as seen in this thesis, for the pre-AGB evolution.

- Formulas from Vassiliadis and Wood (1993): calibrated on observed mass loss rates - pulsation periods relation of the variabile AGB stars.

- The Blöcker's law: characterized by a steep luminosity dependence. The authors assumed a Reimers' formula with $\eta_R = 0.2$ firstly, then the Blöcker's one keeping the same efficiency parameter $\eta_B = 0.2$, as suggested in the original paper Bloecker (1995).

- van Loon et al. (2005): derived from spectroscopic and photometric observations of dust-enshrouded giants in the Large Magellanic Cloud (LMC). The authors adopted the Reimers' law with $\eta_R = 0.2$ and then, when the pulsation period became longer than 300 days, the van Loon's one.

- Their own prescription, taken from the paper Marigo, Bressan, et al. (2013).

For each mass loss proceeding, the authors applied two values for the 3^{rd} dredge-up efficiency $\lambda = 1$ and $\lambda = 0$. The results are exposed in figure 4.6 from Kalirai, Marigo, and Tremblay (2014). Then, through observed constraints, they rejected unsuitable trends for the mass loss efficiency.

They inferred that:

- the width of the area enclosed between the absence of dredge-up and the $\lambda = 1$ value was inversely proportional to the average efficiency of the mass loss (left panel of figure 4.6 on the facing page).

- although the Vassiliadis and Wood (1993) and the Marigo, Bressan, et al. (2013) were calibrated through different quantities (respectively pulsation periods for the first; radii, masses and effective temperatures for the second), they both fit with the observed data.

- Due to the predominant role of the stellar winds, the Bloecker (1995) relation understimated the mass increment. Even assuming no dredge-up, the mass loss was too strong to explain the empirical trend. The van Loon et al. (2005) met a similar fate. On the other hand, the Reimers' law overstimated the core growth (left panel).

- The high efficiency of the Blöcker was driven by the luminosity increase ($\dot{M} \propto L^{4.2}$), instead van Loon was controlled by a steep dependence from the effective temperature ($\dot{M} \propto T_{eff}^{-6.3}$).

- The agreement between observed constraints and predicted trends could be satisfied for almost all the models assuming different parameters: $\eta_R = 2.0$ for the Reimers; $\eta_B = 0.05$ in the Blöcker's; $\eta_{vL} = 0.4$ multiplicative factor included in the val Loon's; delayed super-wind in the Vassiliadis & Wood prescription. The results obtained are shown in the right panel of the figure 4.6 on the preceding page. Comparing the right with the left panel, while the delayed super-wind allowed a slightly better agreement for $M_i \geq 3M_\odot$ for the Vassiliadis & Wood, all the other prescriptions (except for Marigo, Bressan, et al. (2013)) suffered a substantial readjustment. These new proceedings shared a peak at $M_i \simeq 2M_\odot$ and declining wings at both lower and higher masses.

- The comparison of different proceedings could shed light on which process must be definitely considered as the most influent in TP-AGB stellar models. It was clear that, even if the λ efficiency could not be considered as negligible, assuming different mass loss functions caused larger variations.

Table 4.6: Results from Cristallo, Straniero, Piersanti, et al. (2015) analysed for $Z = 0.02$. $M_{initial}$ and M_{final} are respectively the ZAMS mass and the final core mass. $M_{c,1TP}$ is the core mass at the First Thermal Pulse; $M_{c,min}^{3^{rd}du}$ is the core mass at the onset of the 3^{rd} dredge-up; λ_{max} is the maximum value for the efficiency of the 3^{rd} dredge-up. Finally, $\Delta M_{dredge-up}$ is the mass which undergoes dredge-up.

MASS LOSS	$M_{initial}$ $[M_\odot]$	$M_{c,1TP}$ $[M_\odot]$	$M_{c,min}^{3^{rd}du}$ $[M_\odot]$	λ_{max}	$\Delta M_{dredge-up}$	M_{final}
Reimers (1975)	1.3	0.5345	-	0.0000	0.000000	0.6227
	1.5	0.5363	0.5609	0.2077	0.005578	0.6316
Vassiliadis &	2.0	0.5382	0.5530	0.4430	0.029633	0.6293
Wood (1993)	2.5	0.5169	0.5267	0.5211	0.066701	0.6396
	3.0	0.5454	0.5588	0.6014	0.071359	0.6493
	4.0	0.7220	0.7246	0.4603	0.010973	0.7540
	5.0	0.8264	0.8279	0.3656	0.004057	0.8462
	6.0	0.8934	0.8945	0.3297	0.003648	0.9150

Table 4.7: Results from Weiss and Ferguson (2009) analysed for $Z = 0.02$. $M_{initial}$ and M_{final} are respectively the ZAMS mass and the final core mass. $M_{c,1TP}$ is the core mass at the First Thermal Pulse; $M_{c,min}^{3^{rd}du}$ is the core mass at the onset of the 3^{rd} dredge-up.

MASS LOSS	$M_{initial}$ $[M_\odot]$	$M_{c,1TP}$ $[M_\odot]$	$M_{c,min}^{3^{rd}du}$ $[M_\odot]$	M_{final}
Reimers (1975)	1.0	0.501	0.508	0.508
	1.2	0.509	-	0.524
van Loon et al.(2005)	1.5	0.511	0.526	0.539
	1.6	0.508	0.522	0.538
Wachter et al.(2002)	1.8	0.496	0.503	0.524
	2.0	0.478	0.484	0.543
	2.6	0.518	0.533	0.560
	3.0	0.596	0.596	0.617
	4.0	0.765	0.766	0.783
	5.0	0.830	0.831	0.850
	6.0	0.928	0.928	0.937

Table 4.8: Results from A. I. Karakas (2010) analysed for $Z = 0.02$. $M_{initial}$ and M_{final} are respectively the ZAMS mass and the final core mass. $M_{c,1TP}$ is the core mass at the First Thermal Pulse; λ_{max} is the maximum value for the efficiency of the 3^{rd} dredge-up; $\Delta M_{dredge-up}$ is the mass which undergoes dredge-up.

MASS LOSS	$M_{initial}$ $[M_\odot]$	$M_{c,1TP}$ $[M_\odot]$	λ_{max}	$\Delta M_{dredge-up}$	M_{final}
Reimers (1975)	1.00	0.544	0.00	0.00000	0.564
	1.25	0.553	0.00	0.00000	0.574
Vassiliadis &	1.50	0.558	0.00	0.00000	0.593
Wood (1993)	1.75	0.561	0.00	0.00000	0.615
	1.90	0.561	0.00	0.00000	0.630
	2.00	0.553	0.00	0.00000	0.639
	2.25	0.541	0.24	0.00472	0.661
	2.50	0.534	0.56	0.02506	0.658
	3.00	0.576	0.78	0.07928	0.680
	3.50	0.667	0.86	0.10029	0.715
	4.00	0.774	0.98	0.05564	0.793
	4.50	0.840	0.99	0.05269	0.852
	5.00	0.862	0.96	0.05005	0.874
	5.50	0.885	0.96	0.07470	0.900
	6.00	0.915	0.96	0.05813	0.929
	6.50	0.951	0.94	0.04870	0.963

Table 4.9: Results from Marigo, Bressan, et al. (2013) analysed for $Z = 0.02$. $M_{initial}$ and M_{final} are respectively the ZAMS mass and the final core mass. $M_{c,1TP}$ is the core mass at the First Thermal Pulse; $M_{c,min}^{3^{rd}du}$ is the core mass at the onset of the 3^{rd} dredge-up; $\Delta M_{dredge-up}$ is the mass which undergoes dredge-up.

MASS LOSS	$M_{initial}$ $[M_\odot]$	$M_{c,1TP}$ $[M_\odot]$	$M_{c,min}^{3^{rd}du}$ $[M_\odot]$	$\Delta M_{dredge-up}$	M_{final}
Cranmer & Saar (2011)	1.00	0.5184	-	0.00000	0.5396
	1.20	0.5263	-	0.00000	0.5748
Blöcker (1995)	1.40	0.5285	-	0.00000	0.6054
	1.60	0.5278	-	0.00000	0.6322
Mattsson et al. (2010)	1.80	0.5128	-	0.00000	0.6554
	1.90	0.5004	-	0.00000	0.6681
	2.00	0.5038	0.5981	0.00653	0.6753
	2.05	0.5005	0.5948	0.01164	0.6789
	2.10	0.5121	0.5915	0.02197	0.6796
	2.15	0.5123	0.5893	0.02619	0.6818

to be continued

continued

MASS LOSS	$M_{initial}$ $[M_\odot]$	$M_{c,1TP}$ $[M_\odot]$	$M_{c,min}^{3^{rd}du}$ $[M_\odot]$	$\Delta M_{dredge-up}$	M_{final}
	2.20	0.5187	0.5838	0.03341	0.6834
	2.25	0.5208	0.5821	0.03996	0.6857
	2.30	0.5256	0.5818	0.04573	0.6879
	2.40	0.5352	0.5851	0.05786	0.6931
	2.60	0.5668	0.5950	0.07222	0.7079
	2.80	0.5974	0.6121	0.07758	0.7266
	3.00	0.6388	0.6441	0.07100	0.7487
	3.20	0.6805	0.6825	0.05990	0.7734
	3.40	0.7242	0.7242	0.05634	0.7928
	3.60	0.7524	0.7524	0.05095	0.8143
	3.80	0.7629	0.7629	0.05487	0.8274
	4.00	0.7755	0.7755	0.05627	0.8422
	4.20	0.7868	0.7868	0.05973	0.8555
	4.40	0.8043	0.8043	0.05944	0.8731
	4.60	0.8135	0.8135	0.06311	0.8843
	4.80	0.8329	0.8329	0.05977	0.9007
	5.00	0.8470	0.8470	0.05649	0.9119
	5.20	0.8663	0.8663	0.05012	0.9249
	5.40	0.8892	0.8892	0.04304	0.9402
	5.60	0.9117	0.9117	0.03801	0.9561
	5.80	0.9393	0.9393	0.03176	0.9772
	6.00	0.9667	0.9667	0.02609	1.0002

4.2.3 Dependence on Metallicity

Almost all the physical processes involved in the stellar evolution are influenced by the metallicity, hence the dependence on this quantity is the overall result of the dependence of each single process. The general thought is that a lower metallicity corresponds to a higher core mass after the Main Sequence. Unfortunately, the post MS mass loss dependence on Z can not count on a robust theory, but it is thought that at lower metallicity the stellar wind becomes less efficient, hence the TP-AGB phase lasts longer and the core can accrete more material. An important result was gained in the paper Kalirai, Saul Davis, et al. (2009), discussed in the paragraph 5.2 within. In this paper the authors exploited the comparison between metal-poor (M4 or NGC6121, $[Fe/H] = -1.10$) and metal-rich (NGC6791, $[Fe/H] = +0.40$) clusters. They found that at super-solar Z the mass loss was strongly influenced by the metallicity (Kalirai, Bergeron, et al. (2007)), following the expected anti-correlation between Z and core growth; while over the range extending from metal-poor to solar metallicity the mass loss was nearly independent from the

Z. Furthermore, according to A. I. Karakas, Lattanzio, and Pols (2002) the value of the 3^{rd} dredge-up efficiency increases at each thermal pulse during the TP-AGB phase, reaching a maximum λ_{max} which typically increases with the stellar mass and decreases at larger metallicity. We analyse the metallicity dependence showing the tracks predicted by each model for different Z in figure 4.7 on page 45:

- The expected anti-correlation between Z and the remnant mass is confirmed according to Cristallo, Straniero, Piersanti, et al. (2015) (top left-hand side panel) for $M_i \geq 3M_\odot$; at lower masses the suggested IFMR is quite similar for $Z = 0.01$ (blue curve), $Z = 0.014$ (black curve) and $Z = 0.02$ (yellow curve); the $Z = 0.001$ (red) curve respects at every range of mass the expected proceeding.

- Weiss and Ferguson (2009) (top right panel) predict that for initial masses $M_i < 2.6M_\odot$ the $Z = 0.04$ (green line), $Z = 0.02$ (yellow line), $Z = 0.008$ (black line) and $Z = 0.004$ (blue line) curves are nearly similar, except for the $Z = 0.004$ which presents a drop at $M_i = 1.8M_\odot$. It is interesting that a similar drop occurs for $Z = 0.0005$ (red line) at the same initial mass. For larger masses the IFMR follows the expected prediction for all the metallicities considered.

- A. I. Karakas (2010) (bottom left panel) suggests that for $1.5M_\odot \leq M_i \leq 2.5M_\odot$ the $Z = 0.02$ (yellow line),$Z = 0.008$ (black line) and $Z = 0.004$ (blue line) curves are quite similar. In the range $M_i \geq 2.5M_\odot$, for a fixed initial mass a lower Z corresponds to a higher final mass. It is interesting to note that the $Z = 0.008$ track shows a hollow at $M_i = 1.25M_\odot$.

- According to Marigo, Bressan, et al. (2013) (bottom right panel) the $Z = 0.001$ (blue) and $Z = 0.0005$ (red) tracks nearly coincide, both showing a steep slope and a slight hollow at $M_i \simeq 1.6M_\odot$. The $Z = 0.004$ (cyan) track follows a similar proceeding, reaching lower final masses. The $Z = 0.02$ (magenta), $Z = 0.014$ (green) and $Z = 0.008$ (yellow) tracks are quite similar up to $M_i \simeq 1.5M_\odot$. It is interesting to note that in the range $1.5M_\odot < M_i \leq 2.6M_\odot$ for a fixed M_i a lower metallicity corresponds to a lower remnant mass, while the trend is inverted for $M_i \geq 2.6M_\odot$, where the anti-correlation between Z and the final mass is confirmed for all the metallicities considered.

Subsequently, for the chosen $Z = 0.008$, $Z = 0.004$ ($Z = 0.003$ for Cristallo, Straniero, Piersanti, et al. (2015)) and $Z = 0.02$ metallicities we compare the

models (blue curve for Cristallo, Straniero, Piersanti, et al. (2015), yellow curve for Weiss and Ferguson (2009), red curve for A. I. Karakas (2010), green curve for Marigo, Bressan, et al. (2013)) in figure 4.8. Firstly, for $Z = 0.008$ (the upper left graphic), the IFMRs provided by Cristallo, Straniero, Piersanti, et al. (2015) and A. I. Karakas (2010) are in good agreement for $M_i \geq 1.5M_\odot$; Weiss and Ferguson (2009) predict a constant IFMR with lower remnant mass for the range $1M_\odot \leq M_i < 3M_\odot$, then an increasing trend in agreement with Cristallo, Straniero, Piersanti, et al. (2015) and A. I. Karakas (2010) and finally a larger core for $M_i = 6M_\odot$; Marigo, Bressan, et al. (2013) suggest a steep slope for the IFMR which starts from $M_f = 0.4828M_\odot$ at $M_i = 0.5M_\odot$ and it ends with a final mass of about $1M_\odot$ for $M_i = 5.6M_\odot$.

Considering $Z = 0.004$ (for Cristallo, Straniero, Piersanti, et al. (2015) we use $Z = 0.003$) in the upper right graphic, we note that the agreement between A. I. Karakas (2010) and Cristallo, Straniero, Piersanti, et al. (2015) is even stronger up to $M_i = 5M_\odot$; the track provided by Weiss and Ferguson (2009) is still significantly lower for $1M_\odot \leq M_i \leq 2M_\odot$, showing a drop at $M_i = 1.8M_\odot$, before it connects with the other models as for $Z = 0.008$; Marigo, Bressan, et al. (2013) predict a steeper slope for the proceeding, which starts from $M_f = 0.4884$ at $M_i = 0.505M_\odot$ and it reachs $M_f = 1.0145M_\odot$ at $M_i = 5.4M_\odot$. Considering the sup-solar metallicity $Z = 0.02$, exposed in the bottom panel, Cristallo, Straniero, Piersanti, et al. (2015) suggest a nearly constant IFMR up to $M_i = 3M_\odot$ followed by an increasing trend; the track taken from A. I. Karakas (2010) is similar to that of Cristallo, Straniero, Piersanti, et al. (2015) for $M_i \geq 2M_\odot$, but the remnant mass predicted is larger; Weiss and Ferguson (2009) assume a weaker core growth for $1M_\odot \leq M_i < 3M_\odot$ with shallower drop which occurs at $M_i = 1.8M_\odot$; according to Marigo, Bressan, et al. (2013) the IFMR shows a steep slope up to $M_i = 2M_\odot$, then a plateau in the range $2M_\odot \leq M_i \leq 2.4M_\odot$ and finally a further increasing trend.

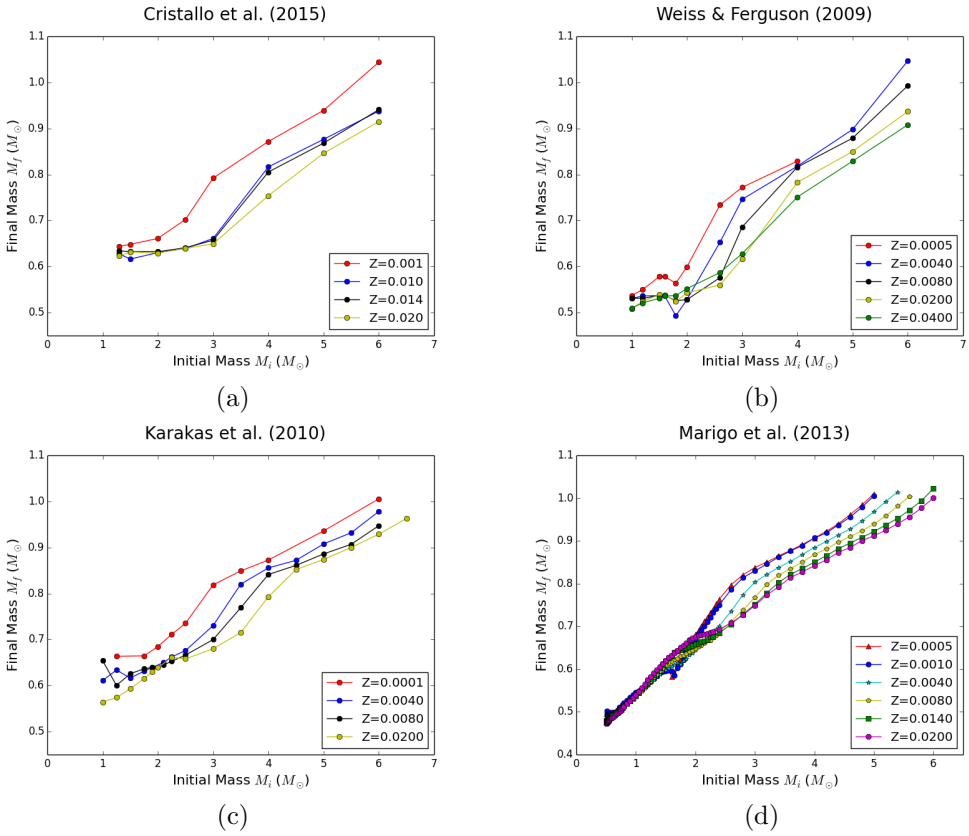

Figure 4.7: IFMR according to Cristallo, Straniero, Piersanti, et al. (2015) (figure (a)), Weiss and Ferguson (2009) (figure (b)), A. I. Karakas (2010) (figure (c)), Marigo, Bressan, et al. (2013) (figure (d)).

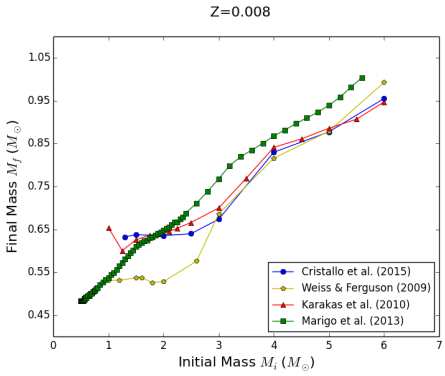

(a) $Z = 0.008$.

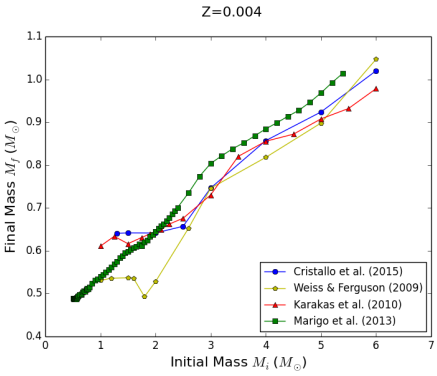

(b) $Z = 0.004$.

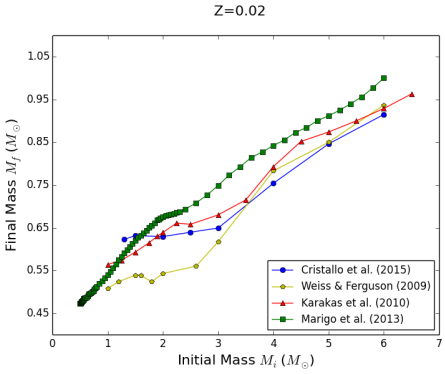

(c) $Z = 0.02$.

Figure 4.8: Predicted models for $Z = 0.008$ (figure (a)), $Z = 0.004$ (figure (b)) and $Z = 0.02$ (figure (c)).

4.3 Testing Models

We can finally compare the predicted to the semi-empirical (exposed in table 3.1) IFMRs to put some constraints on the TP-AGB phase. In figure 4.9 on the next page we show the results using the $Z = 0.02$ models. The solid lines represent the predicted remnant mass, while the dashed lines show the final masses as if the 3^{rd} dredge-up would never occur (see the section 4.2.1). We immediately observe that Cristallo, Straniero, Piersanti, et al. (2015),Weiss and Ferguson (2009) and A. I. Karakas (2010) understimate the core growth for $M_i \geq 3M_\odot$. For lower masses $M_i \leq 3M_\odot$, Weiss and Ferguson (2009) and Cristallo, Straniero, Piersanti, et al. (2015) predict a nearly constant IFMR instead of the steep increasing trend observed. Furthermore, no author includes the flattening observed at $M_i = 4M_\odot$. The IFMR proposed by Marigo, Bressan, et al. (2013) fits the semi-empirical data up to about $3M_\odot$, but for larger initial masses this model understimates the remnant masses too. It is interesting to note that assuming a small value for the 3^{rd} dredge-up efficiency λ (the dashed lines) in models for $M_i \geq 2M_\odot$ stars can improve significantly the agreement with the semi-empirical IFMR.

In figure 4.10 on the following page we compare the semi-empirical IFMR with models provided by Cristallo, Straniero, Piersanti, et al. (2015) (cyan line) and Marigo, Bressan, et al. (2013) (green line) for $Z = 0.014$, since a lower metallicity is thought to correspond to higher remnant masses, as explained in section 4.2.3 on page 42. For Cristallo, Straniero, Piersanti, et al. (2015) the core growth is still too weak for $M_i \geq 3M_\odot$, and the trend at lower masses seems to be unsuitable. The model provided by Marigo, Bressan, et al. (2013) slightly improves for $M_i \geq 3M_\odot$; however, according to the correlation between Z and M_f assumed for $1.5M_\odot < M_i \leq 2.6M_\odot$ (see figure 4.7 on page 45), the trend gets worse and it can't fit the semi-empirical IFMR.

Finally we want to stress that even if we focused only on the 3^{rd} dredge-up varying the λ parameter to improve the agreement between semi-empirical and predicted IFMRs, the model proposed by A. I. Karakas (2010) couldn't match even considering a weak stellar wind: indeed, since the core does not increase due to the large λ assumed, the effects of the stellar wind and the 3^{rd} dredge-up are disentagled.

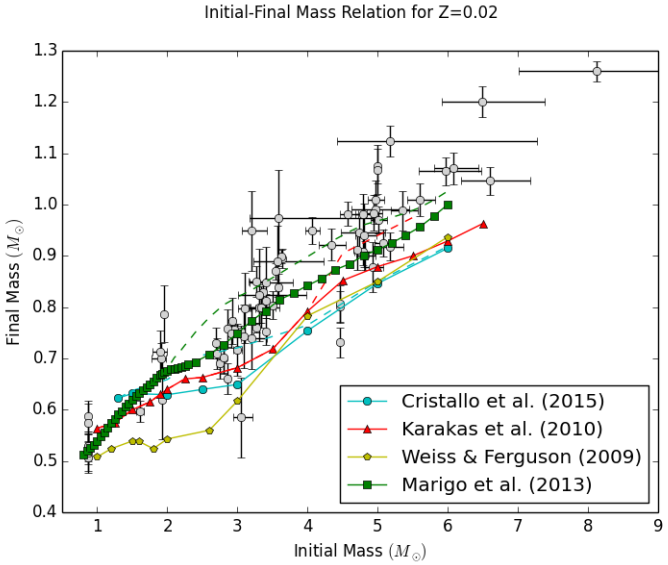

Figure 4.9: Predicted IFMRs applied to the semi-empirical IFMR (table 3.1 on page 21).

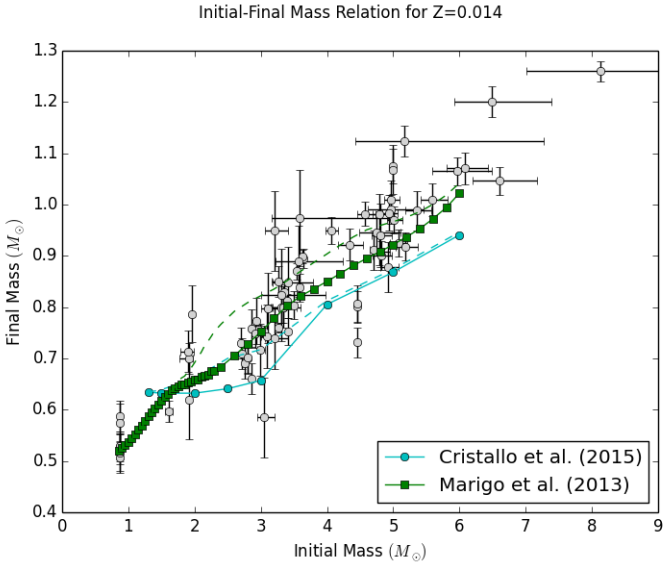

Figure 4.10: Predicted IFMRs provided by Cristallo, Straniero, Piersanti, et al. (2015) (cyan line) and Marigo, Bressan, et al. (2013) (green line) applied to the semi-empirical IFMR (table 3.1 on page 21).

Chapter 5

Summary and Conclusions

The IFMR for low- and intermediate-mass stars ($0.9M_{\odot} \leq M_i \leq 6-9M_{\odot}$) is a fundamental tool for both stellar evolution analysis and galaxy models: it gives an upper value for the initial mass of stars developing a CO core, thus it becomes a test for Type Ia (Marigo (2013)) and Type II (Kalirai, Hansen, et al. (2008)) Supernovae rates; it puts constraints to the amount of metal-enriched gas ejected to the interstellar medium; it can be used to determine the age and distance of globular cluster interpreting the luminosity function and modeling the cooling sequence of the WDs; it provides an estimate of the luminosity contribution of the TP-AGB star population to the integrated galaxy light.

In the last years the relation has been improving due to the step forward made by both theoretical models and observations; however, the use of theoretical models brings unavoidable systematic errors (see Salaris et al. (2009)) to the cluster's age, metallicity, amount of convective overshooting, thickness of the WD H/He layers, chemical composition of the degenerate core (Marigo (2013)) which make the scatter in the relation larger.

Thus, the semi-empirical IFMR (figure 3.2 on page 24) shows a monotonically increasing trend, with a supposed local maximum at $M_i = 2M_{\odot}$ and a flattening at $M_i \simeq 4M_{\odot}$. The stellar evolution theory suggests the transition from low-mass, which develop an electron degenerate He-core after H-burning phase, to intermediate-mass stars, which avoid the He-flash, at $2M_{\odot}$. Moreover, the $M_i = 2M_{\odot}$ marks the minimum mass to experience the 3^{rd} dredge-up at $Z = 0.02$. Instead, the flattening at $\sim 4M_{\odot}$ can be a hint of the occurence of the 2^{nd} dredge-up during the Early-AGB phase. If true, the IFMR could provide a direct observation of this event. Hence, these masses must be further investigated to infer their respectively influences in the core growth.

In this thesis we focus on three main factors that affect the AGB phase and their supposed effects: the 3^{rd} *dredge-up*, which prevents the core growth

subtracting material that would otherwise accrete the core; the *mass loss*, which drives the duration of the AGB phase itself; the *metallicity*, which controls the efficiency of each process involved in the AGB phase. To infer the role of each process in the core growth, we test at different metallicities Z four theoretical predicted IFMRs provided by different authors: Cristallo, Straniero, Piersanti, et al. (2015),Weiss and Ferguson (2009), A. I. Karakas (2010) and Marigo, Bressan, et al. (2013).

The IFMR dependence on the 3^{rd} dredge-up is measured through the efficiency λ (formula 2.1 on page 11): a larger λ value makes the core mass growth less efficient (figures 4.4 on page 34 and 4.5 on page 35).

The mass loss limits the duration of the AGB phase because a stronger stellar wind makes the phase shorter and thus the core has less time to increase. In this thesis we assume the results inferred by Kalirai, Marigo, and Tremblay (2014), in particular the primary role played by the mass loss in the core growth: indeed, even if the λ efficiency could not be considered as negligible, assuming different mass loss functions causes larger variations.

Finally, for a fixed initial mass a lower metallicity corresponds to higher final mass. This trend is generally confirmed for all the models used (figure 4.7 on page 45).

Subsequently we compare the semi-empirical data provided by prof. Jeffrey D. Cummings (private communication) with models at $Z = 0.02$ (figure 4.9 on page 48) and $Z = 0.014$ (figure 4.10 on page 48), showing a qualitative agreement in the trend for A. I. Karakas (2010) and Marigo, Bressan, et al. (2013), but significant differences in the quantitative predictions: all the models understimate the remnant mass for $M_i \geq 3M_\odot$ and only the prescription provided by Marigo, Bressan, et al. (2013) for $Z = 0.02$ fits the semi-empirical data for $M_i \leq 3M_\odot$. However, the comparison provides important hints towards a lower efficiency of the 3^{rd} dredge-up in massive AGB stars than in standard calculations at both $Z = 0.02$ and $Z = 0.014$: indeed, $\lambda \sim 1$, as predicted by A. I. Karakas (2010), seems to be unsuitable. This may have critical implications for the chemical yields produced by massive stars undergoing Hot Bottom Burning, so that the CNO, Ne−Na and Mg−Al cycles (Forestini and Charbonnel (1997)), and s-process nucleosynthesis.

Bibliography

Althaus, L. G. et al. (2007). "The age and colors of massive white dwarf stars". In: 465, pp. 249–255. DOI: 10.1051/0004-6361:20066059. eprint: astro-ph/0702024.

Anders, E. and N. Grevesse (1989). "Abundances of the elements - Meteoritic and solar". In: 53, pp. 197–214. DOI: 10.1016/0016-7037(89)90286-X.

Bergeron, P., R. A. Saffer, and J. Liebert (1992). "A spectroscopic determination of the mass distribution of DA white dwarfs". In: 394, pp. 228–247. DOI: 10.1086/171575.

Bessell, M. S. et al. (1989). "Colors of extended static model photospheres of M giants". In: 77, pp. 1–30.

Bloecker, T. (1995). "Stellar evolution of low and intermediate-mass stars. I. Mass loss on the AGB and its consequences for stellar evolution." In: 297, p. 727.

Bloecker, T. and D. Schoenberner (1991). "A 7-solar-mass AGB model sequence not complying with the core mass-luminosity relation". In: 244, pp. L43–L46.

Bressan, A. et al. (2012). "PARSEC: stellar tracks and isochrones with the PAdova and TRieste Stellar Evolution Code". In: 427, pp. 127–145. DOI: 10.1111/j.1365-2966.2012.21948.x. arXiv: 1208.4498 [astro-ph.SR].

Caffau, E. et al. (2011). "Solar Chemical Abundances Determined with a CO5BOLD 3D Model Atmosphere". In: 268, pp. 255–269. DOI: 10.1007/s11207-010-9541-4. arXiv: 1003.1190 [astro-ph.SR].

Chieffi, A., M. Limongi, and O. Straniero (1998). "The Evolution of a 25 M Star from the Main Sequence up to the Onset of the Iron Core Collapse". In: 502, pp. 737–762. DOI: 10.1086/305921.

Chiosi, C., P. R. Wood, and N. Capitanio (1993). "Theoretical models of Cepheid variables and their BVI(c) colors and magnitudes". In: 86, pp. 541–598. DOI: 10.1086/191790.

Claver, C. F. et al. (2001). "The Masses of White Dwarfs in the Praesepe Open Cluster". In: 563, pp. 987–998. DOI: 10.1086/323792.

Cranmer, S. R. and S. H. Saar (2011). "Testing a Predictive Theoretical Model for the Mass Loss Rates of Cool Stars". In: 741, 54, p. 54. DOI: 10.1088/0004-637X/741/1/54. arXiv: 1108.4369 [astro-ph.SR].

Cristallo, S., L. Piersanti, et al. (2011). "Evolution, Nucleosynthesis, and Yields of Low-mass Asymptotic Giant Branch Stars at Different Metallicities. II. The FRUITY Database". In: 197, 17, p. 17. DOI: 10.1088/0067-0049/197/2/17. arXiv: 1109.1176 [astro-ph.SR].

Cristallo, S., O. Straniero, R. Gallino, et al. (2009). "Evolution, Nucleosynthesis, and Yields of Low-Mass Asymptotic Giant Branch Stars at Different Metallicities". In: 696, pp. 797–820. DOI: 10.1088/0004-637X/696/1/797. arXiv: 0902.0243 [astro-ph.SR].

Cristallo, S., O. Straniero, L. Piersanti, et al. (2015). "Evolution, Nucleosynthesis, and Yields of AGB Stars at Different Metallicities. III. Intermediate-mass Models, Revised Low-mass Models, and the ph-FRUITY Interface". In: 219, 40, p. 40. DOI: 10.1088/0067-0049/219/2/40. arXiv: 1507.07338 [astro-ph.SR].

Cummings, J. D., J. S. Kalirai, P.-E. Tremblay, and E. Ramirez-Ruiz (2015). "Initial-Final Mass Relation for 3 to 4 M Progenitors of White Dwarfs from the Single Cluster NGC 2099". In: 807, 90, p. 90. DOI: 10.1088/0004-637X/807/1/90. arXiv: 1505.06737 [astro-ph.SR].

— (2016). "Two Massive White Dwarfs from NGC 2323 and the Initial-Final Mass Relation for Progenitors of 4 to 6.5 M". In: 818, 84, p. 84. DOI: 10.3847/0004-637X/818/1/84. arXiv: 1601.03053 [astro-ph.SR].

Cummings, J. D., J. S. Kalirai, P.-E. Tremblay, E. Ramirez-Ruiz, and P. Bergeron (2016). "An Ultramassive 1.28 M_{2299} White Dwarf in NGC 2099". In: 820, L18, p. L18. DOI: 10.3847/2041-8205/820/1/L18. arXiv: 1603.00471 [astro-ph.SR].

Dominguez, I. et al. (1999). "Intermediate-Mass Stars: Updated Models". In: 524, pp. 226–241. DOI: 10.1086/307787. eprint: astro-ph/9906030.

Ferguson, J. W. et al. (2005). "Low-Temperature Opacities". In: 623, pp. 585–596. DOI: 10.1086/428642. eprint: astro-ph/0502045.

Fontaine, G., P. Brassard, and P. Bergeron (2001). "The Potential of White Dwarf Cosmochronology". In: 113, pp. 409–435. DOI: 10.1086/319535.

Forestini, M. and C. Charbonnel (1997). "Nucleosynthesis of light elements inside thermally pulsing AGB stars: I. The case of intermediate-mass stars". In: 123, pp. 241–272. DOI: 10.1051/aas:1997348.

Herwig, F. (2005). "Evolution of Asymptotic Giant Branch Stars". In: 43, pp. 435–479. DOI: 10.1146/annurev.astro.43.072103.150600.

Hurley, J. R., O. R. Pols, and C. A. Tout (2000). "Comprehensive analytic formulae for stellar evolution as a function of mass and metallicity". In:

315, pp. 543–569. DOI: 10.1046/j.1365-8711.2000.03426.x. eprint: astro-ph/0001295.

Iben Jr., I. and J. W. Truran (1978). "On the surface composition of thermally pulsing stars of high luminosity and on the contribution of such stars to the element enrichment of the interstellar medium". In: 220, pp. 980–995. DOI: 10.1086/155986.

Iglesias, C. A. and F. J. Rogers (1996). "Updated Opal Opacities". In: 464, p. 943. DOI: 10.1086/177381.

Kalirai, J. S., P. Bergeron, et al. (2007). "Stellar Evolution in NGC 6791: Mass Loss on the Red Giant Branch and the Formation of Low-Mass White Dwarfs". In: 671, pp. 748–760. DOI: 10.1086/521922. arXiv: 0705.0977.

Kalirai, J. S., G. G. Fahlman, et al. (2003). "The CFHT Open Star Cluster Survey. IV. Two Rich, Young Open Star Clusters: NGC 2168 (M35) and NGC 2323 (M50)". In: 126, pp. 1402–1414. DOI: 10.1086/377320. eprint: astro-ph/0306241.

Kalirai, J. S., B. M. S. Hansen, et al. (2008). "The Initial-Final Mass Relation: Direct Constraints at the Low-Mass End". In: 676, 594-609, pp. 594–609. DOI: 10.1086/527028. arXiv: 0706.3894.

Kalirai, J. S., P. Marigo, and P.-E. Tremblay (2014). "The Core Mass Growth and Stellar Lifetime of Thermally Pulsing Asymptotic Giant Branch Stars". In: 782, 17, p. 17. DOI: 10.1088/0004-637X/782/1/17. arXiv: 1312.4544 [astro-ph.SR].

Kalirai, J. S., H. B. Richer, G. G. Fahlman, et al. (2001). "The CFHT Open Star Cluster Survey. II. Deep CCD Photometry of the Old Open Star Cluster NGC 6819". In: 122, pp. 266–282. DOI: 10.1086/321141. eprint: astro-ph/0104164.

Kalirai, J. S., H. B. Richer, D. Reitzel, et al. (2005). "The Initial-Final Mass Relationship: Spectroscopy of White Dwarfs in NGC 2099 (M37)". In: 618, pp. L123–L127. DOI: 10.1086/427774.

Kalirai, J. S., D. Saul Davis, et al. (2009). "The Masses of Population II White Dwarfs". In: 705, pp. 408–425. DOI: 10.1088/0004-637X/705/1/408. arXiv: 0909.2253 [astro-ph.SR].

Kalirai, J. S., P. Ventura, et al. (2001). "The CFHT Open Star Cluster Survey. III. The White Dwarf Cooling Age of the Rich Open Star Cluster NGC 2099 (M37)". In: 122, pp. 3239–3257. DOI: 10.1086/324463. eprint: astro-ph/0109368.

Karakas, A. I. (2010). "Updated stellar yields from asymptotic giant branch models". In: 403, pp. 1413–1425. DOI: 10.1111/j.1365-2966.2009.16198.x. arXiv: 0912.2142 [astro-ph.SR].

Karakas, A. I., J. C. Lattanzio, and O. R. Pols (2002). "Parameterising the Third Dredge-up in Asymptotic Giant Branch Stars". In: 19, pp. 515–526. DOI: 10.1071/AS02013. eprint: astro-ph/0210058.

Karakas, A. and J. C. Lattanzio (2007). "Stellar Models and Yields of Asymptotic Giant Branch Stars". In: 24, pp. 103–117. DOI: 10.1071/AS07021. arXiv: 0708.4385.

Lederer, M. T. and B. Aringer (2009). "Low temperature Rosseland opacities with varied abundances of carbon and nitrogen". In: 494, pp. 403–416. DOI: 10.1051/0004-6361:200810576. arXiv: 0810.5672.

Liebert, J. et al. (2005). "The Age and Progenitor Mass of Sirius B". In: 630, pp. L69–L72. DOI: 10.1086/462419. eprint: astro-ph/0507523.

Lodders, K. (2003). "Solar System Abundances and Condensation Temperatures of the Elements". In: 591, pp. 1220–1247. DOI: 10.1086/375492.

Marigo, P. (2002). "Asymptotic Giant Branch evolution at varying surface C/O ratio: effects of changes in molecular opacities". In: 387, pp. 507–519. DOI: 10.1051/0004-6361:20020304. eprint: astro-ph/0203036.

— (2013). "Asymptotic Giant Branch Evolution and the Initial-Final Mass Relation of Single CO White Dwarfs". In: *Binary Paths to Type Ia Supernovae Explosions*. Ed. by R. Di Stefano, M. Orio, and M. Moe. Vol. 281. IAU Symposium, pp. 36–43. DOI: 10.1017/S1743921312014664.

— (2015). "Approaching a Physical Calibration of the AGB Phase". In: *IAU General Assembly* 22, 2257393, p. 2257393.

Marigo, P. and B. Aringer (2009). "Low-temperature gas opacity. ÆSOPUS: a versatile and quick computational tool". In: 508, pp. 1539–1569. DOI: 10.1051/0004-6361/200912598. arXiv: 0907.3248 [astro-ph.SR].

Marigo, P., A. Bressan, et al. (2013). "Evolution of thermally pulsing asymptotic giant branch stars - I. The COLIBRI code". In: 434, pp. 488–526. DOI: 10.1093/mnras/stt1034. arXiv: 1305.4485 [astro-ph.SR].

Marigo, P. and L. Girardi (2007). "Evolution of asymptotic giant branch stars. I. Updated synthetic TP-AGB models and their basic calibration". In: 469, pp. 239–263. DOI: 10.1051/0004-6361:20066772. eprint: astro-ph/0703139.

Mattsson, L., R. Wahlin, and S. Höfner (2010). "Dust driven mass loss from carbon stars as a function of stellar parameters . I. A grid of solar-metallicity wind models". In: 509, A14, A14. DOI: 10.1051/0004-6361/200912084. arXiv: 0909.1513 [astro-ph.SR].

Mestel, L. (1952). "On the theory of white dwarf stars. I. The energy sources of white dwarfs". In: 112, p. 583. DOI: 10.1093/mnras/112.6.583.

Perryman, M. A. C. et al. (1998). "The Hyades: distance, structure, dynamics, and age". In: 331, pp. 81–120. eprint: astro-ph/9707253.

Rosenfield, P. et al. (2014). "Evolution of Thermally Pulsing Asymptotic Giant Branch Stars. IV. Constraining Mass loss and Lifetimes of Low Mass, Low Metallicity AGB Stars". In: 790, 22, p. 22. DOI: 10.1088/0004-637X/790/1/22. arXiv: 1406.0676 [astro-ph.SR].

Salaris, M. et al. (2009). "Semi-empirical White Dwarf Initial-Final Mass Relationships: A Thorough Analysis of Systematic Uncertainties Due to Stellar Evolution Models". In: 692, pp. 1013–1032. DOI: 10.1088/0004-637X/692/2/1013. arXiv: 0807.3567.

Seaton, M. J. et al. (1992). "The Opacity Project - Computation of Atomic Data". In: 23.

Tremblay, P.-E. and P. Bergeron (2009). "Spectroscopic Analysis of DA White Dwarfs: Stark Broadening of Hydrogen Lines Including Nonideal Effects". In: 696, pp. 1755–1770. DOI: 10.1088/0004-637X/696/2/1755. arXiv: 0902.4182 [astro-ph.SR].

van Loon, J. T. et al. (2005). "An empirical formula for the mass-loss rates of dust-enshrouded red supergiants and oxygen-rich Asymptotic Giant Branch stars". In: 438, pp. 273–289. DOI: 10.1051/0004-6361:20042555. eprint: astro-ph/0504379.

VandenBerg, D. A., P. A. Bergbusch, and P. D. Dowler (2006). "The Victoria-Regina Stellar Models: Evolutionary Tracks and Isochrones for a Wide Range in Mass and Metallicity that Allow for Empirically Constrained Amounts of Convective Core Overshooting". In: 162, pp. 375–387. DOI: 10.1086/498451. eprint: astro-ph/0510784.

Vassiliadis, E. and P. R. Wood (1993). "Evolution of low- and intermediate-mass stars to the end of the asymptotic giant branch with mass loss". In: 413, pp. 641–657. DOI: 10.1086/173033.

Ventura, P. and F. D'Antona (2005). "Full computation of massive AGB evolution. I. The large impact of convection on nucleosynthesis". In: 431, pp. 279–288. DOI: 10.1051/0004-6361:20041917. eprint: astro-ph/0411191.

Wachter, A. et al. (2002). "An improved mass-loss description for dust-driven superwinds and tip-AGB evolution models". In: 384, pp. 452–459. DOI: 10.1051/0004-6361:20020022.

Weiss, A. and J. W. Ferguson (2009). "New asymptotic giant branch models for a range of metallicities". In: 508, pp. 1343–1358. DOI: 10.1051/0004-6361/200912043. arXiv: 0903.2155 [astro-ph.SR].